

















A heterotypic assembly mechanism regulates CHIP E3 ligase activity

Aniruddha Das¹ , Pankaj Thapa¹ , Ulises Santiago² , Nilesh Shanmugam¹ ,
Katarzyna Banasiak¹ , Katarzyna Dąbrowska³ , Hendrik Nolte^{4,†} , Natalia A Szulc¹ ,
Rose M Gathungu⁵ , Dominik Cysewski³ , Marcus Krüger^{4,6} , Michał Dadlez³ ,
Marcin Nowotny⁷ , Carlos J Camacho² , Thorsten Hoppe^{4,6}  & Wojciech Pokrzywa^{1,*} 

Abstract

CHIP (C-terminus of Hsc70-interacting protein) and its worm ortholog CHN-1 are E3 ubiquitin ligases that link the chaperone system with the ubiquitin-proteasome system (UPS). CHN-1 can cooperate with UFD-2, another E3 ligase, to accelerate ubiquitin chain formation; however, the basis for the high processivity of this E3s set has remained obscure. Here, we studied the molecular mechanism and function of the CHN-1–UFD-2 complex in *Caenorhabditis elegans*. Our data show that UFD-2 binding promotes the cooperation between CHN-1 and ubiquitin-conjugating E2 enzymes by stabilizing the CHN-1 U-box dimer. However, HSP70/HSP-1 chaperone outcompetes UFD-2 for CHN-1 binding, thereby promoting a shift to the autoinhibited CHN-1 state by acting on a conserved residue in its U-box domain. The interaction with UFD-2 enables CHN-1 to efficiently ubiquitylate and regulate *S*-adenosylhomocysteinase (AHCY-1), a key enzyme in the *S*-adenosylmethionine (SAM) regeneration cycle, which is essential for SAM-dependent methylation. Our results define the molecular mechanism underlying the synergistic cooperation of CHN-1 and UFD-2 in substrate ubiquitylation.

Keywords *C. elegans*; CHIP/STUB1/CHN-1; metabolism; ubiquitin ligase; UFD-2

Subject Categories Post-translational Modifications & Proteolysis; Translation & Protein Quality

DOI 10.15252/embj.2021109566 | Received 26 August 2021 | Revised 25 May 2022 | Accepted 27 May 2022 | Published online 28 June 2022

The EMBO Journal (2022) 41: e109566

Introduction

The ubiquitin-proteasome system (UPS) comprises a well-studied enzymatic cascade that transfers the small protein ubiquitin (Ub)

onto a protein substrate (Kerscher *et al*, 2006). The last step in the UPS enzymatic cascade is mediated by ubiquitin ligases (E3s), the largest and most diverse group of proteins within the UPS, which are responsible for substrate selection and specificity (Komander, 2009; Buetow & Huang, 2016). Mechanistically, two classes of E3 enzymes are commonly found. HECT (homologous to E6AP C-terminus) E3s form an intermediate thioester bond with ubiquitin before catalyzing substrate ubiquitylation. By contrast, RING (Really Interesting New Gene)/U-box E3s form molecular scaffolds that bring E2-Ub and the target protein into proximity, thereby facilitating direct Ub transfer to the latter (Wenzel *et al*, 2011; Riley *et al*, 2013; Buetow & Huang, 2016). In some instances, other proteins, called ubiquitin chain elongation factors, or E4s, may be required to achieve efficient poly-ubiquitylation of substrates. The first E4 described was yeast Ufd2p (Richly *et al*, 2005), a U-box domain-containing protein that engages Ub via its N-terminal region, thus enhancing Ub chain elongation on a pre-ubiquitylated substrate (Koegele *et al*, 1999; Hatakeyama *et al*, 2001; Buetow & Huang, 2016). Although higher eukaryotes, including humans, have an ortholog of yeast Ufd2p, its Ub-interacting motif has little sequence homology (Hänzelmann *et al*, 2010; Liu *et al*, 2017), suggesting that the function of UFD-2 as an E4 is not evolutionarily conserved.

Early *Caenorhabditis elegans* studies showed that UFD-2 interacts directly with CHN-1 (the nematode ortholog of mammalian CHIP) to form an E3-E4 complex that can efficiently oligo-ubiquitylate the myosin chaperone UNC-45 (Hoppe *et al*, 2004). CHIP (C-terminus of Hsc70-interacting protein), initially identified as a tetratricopeptide repeat (TPR) protein that interacts with heat shock proteins (Ballinger *et al*, 1999), is a U-box E3 ubiquitin ligase that mediates ubiquitylation of chaperone client proteins, promoting their degradation (Murata *et al*, 2001; Paul & Ghosh, 2014; Joshi *et al*, 2016). In contrast to the model proposed based on these early findings,

1 Laboratory of Protein Metabolism, International Institute of Molecular and Cell Biology in Warsaw, Warsaw, Poland

2 Department of Computational and Systems Biology, University of Pittsburgh, Pittsburgh, PA, USA

3 Institute of Biochemistry and Biophysics, PAS, Warsaw, Poland

4 Institute for Genetics and Cologne Excellence Cluster on Cellular Stress Responses in Aging-Associated Diseases (CECAD), University of Cologne, Cologne, Germany

5 Metabolomics Core Facility, EMBL, Heidelberg, Germany

6 Center for Molecular Medicine (CMMC), Faculty of Medicine, University Hospital of Cologne, Cologne, Germany

7 Laboratory of Protein Structure, International Institute of Molecular and Cell Biology in Warsaw, Warsaw, Poland

*Corresponding author. Tel: +48 225970743; E-mail: wpokrzywa@iimcb.gov.pl

†Present address: Max-Planck-Institute for Biology of Ageing, Cologne, Germany

more recent studies have revealed that UFD-2 acts as a true E3 ligase that poly-ubiquitylates UNC-45 independent of CHN-1, suggesting that both UFD-2 and CHN-1 act as E3s in the same or an overlapping substrate space (Hellerschmied *et al*, 2018). A recent study aimed at identifying substrates of human CHIP and the human UFD-2 ortholog UBE4B supports the possibility of shared substrate scope (Bhuripanyo *et al*, 2018). Nevertheless, despite the key role of CHIP/CHN-1 in protein quality control networks, little is known about the regulation of its activity and its interaction with UFD-2, as well as the functional role of this E3 pair.

To address these questions, we combined *in vitro* and *in vivo* assays with computational approaches and lipidomic and proteomic studies in *C. elegans* to uncover the mechanism that controls CHN-1 activity. The crystal structure of murine CHIP bound to the C-terminal decapeptide of the HSP90 chaperone via the TPR domain revealed an asymmetric dimerization in which the two CHIP protomers adopt a “closed” conformation that restricts E2 access to one of the U-box domains, and thus E3 activity (Zhang *et al*, 2005). Subsequent molecular modeling of mouse CHIP indicates dynamics between symmetric and asymmetric autoinhibited dimers, which can be regulated by binding proteins (Ye *et al*, 2017). Our results show that although metazoan UFD-2 lacks E4 activity, it acts as a pre-conditioning factor to influence the conformational flexibility of CHN-1, thus boosting its processivity. Mechanistically, UFD-2 binding to the TPR domain stabilizes the open conformation of CHN-1, allowing the U-box dimer to discharge more Ub-conjugating enzymes (E2) in a single ubiquitylation cycle. We also demonstrated that the heat-shock protein HSP70/HSP-1 interacts with the TPR and U-box domains of CHN-1 to stabilize the closed/auto-inhibitory state of the CHN-1 dimer, thus limiting its interaction with E2 and UFD-2. Furthermore, we identified potential substrates for the CHN-1–UFD-2 pair, including *S*-adenosylhomocysteinase (AHCY-1), a metabolic enzyme previously not known to be a client of heat-shock proteins. However, the UFD-2-dependent increase in CHN-1 processivity and consequent CHN-1 auto-ubiquitylation (auto-Ub) also lead to CHN-1 turnover, thereby reducing organismal proteostasis capacity. Collectively, our results indicate an interplay between chaperones and UFD-2 in modulating CHN-1 activity. This processivity-switching behavior of CHN-1 has important implications for its roles in regulating proteostasis, metabolism, and potentially other cellular processes.

Results

UFD-2 promotes CHN-1 processivity and its cooperation with E2s

Binding between CHN-1 and UFD-2 was previously demonstrated via yeast two-hybrid and *in vitro* pull-down assays (Hoppe *et al*, 2004). Beyond the physical interaction, the molecular regulation of the potent ubiquitylation activity of the CHN-1–UFD-2 complex has not yet been studied in detail. A quantitative assessment of an E3 ligase activity is generally performed by examining its auto-ubiquitylation (auto-Ub) ability. For this purpose, an *in vitro* ubiquitylation assay with recombinant E1, E2, Ub, and E3 proteins with an ATP source can be used. The activity of the E3 enzyme can then be determined via Western blot analysis using antibodies against ubiquitin ligase or Ub itself. First, we chose E2 conjugating

enzymes with which CHN-1 and UFD-2 are known to cooperate in the auto-Ub reaction. Mammalian CHIP can interact with various E2s, particularly from the UbcH5/UBE2D family (UbcH5a/UBE2D1, -b/2, and -c/3) (Jiang *et al*, 2001; Soss *et al*, 2011). Similarly, CHN-1 cooperates with UBE2D2 to mono-ubiquitylate (mono-Ub) *C. elegans* DAF-2, the nematode insulin/insulin-like growth factor 1 (IGF-1) receptor (Tawo *et al*, 2017). To study the activity of CHN-1 and UFD-2, we compared their abilities to auto-Ub in the presence of each of the UBE2D-family proteins. We observed that CHN-1 interacted most efficiently with UBE2D1 and least efficiently with UBE2D3, whereas UFD-2 interacts similarly with UBE2D1-3 (Fig EV1A and B). When we performed an auto-Ub reaction with both E3s, we observed a significant increase in CHN-1 poly-ubiquitylation (poly-Ub) activity, even when the E2 used in the reaction was UBE2D2 or UBE2D3, with which CHN-1 alone inefficiently cooperates (Figs 1A and EV1A). The presence of UFD-2 in the reaction also potentiated CHN-1 auto-Ub with LET-70, the *C. elegans* ortholog of UBE2D proteins (Fig EV1C). Furthermore, the presence of UFD-2 increased CHN-1 activity with the UBE2N-Uev1a E2 complex (Fig EV1D), which catalyzes the formation of free Ub chains that are then transferred to substrate proteins (Soss *et al*, 2011). We also concluded that the induction of E3 ligase activity is unidirectional as we did not detect any significant changes in the auto-Ub of UFD-2 under the same conditions (Fig EV1E). Interestingly, UFD-2 did not interact with UBE2N-Uev1a, indicating specificity between E2s with U-box domain-containing E3s (Fig EV1D and E). We also ruled out the possibility that it was UFD-2 that modified CHN-1 because it was unable to ubiquitylate inactive CHN-1^{H218Q}, which probably lost its affinity toward its cognate E2 (Tawo *et al*, 2017) (Fig EV1F). However, we noted that CHN-1^{H218Q} was modified specifically in the presence of an inactive, recombinant UFD-2 mutant with a P951A substitution (Ackermann *et al*, 2016) (bands marked with an asterisk), which might suggest recovery of CHN-1^{H218Q} minimal activity, reflecting possible structural changes in the CHN-1 U-box domain during an interaction with UFD-2.

To gain insight into CHN-1 processivity, we performed time-dependent auto-Ub experiments (with reaction times of 10, 20, 40, 80, and 120 min). We observed that the presence of UFD-2 increased both mono- and poly-Ub of CHN-1 from the 40-min time point (Fig 1A). When we included the UBE2D2 or UBE2D3 E2s in the reaction, which CHN-1 does not efficiently utilize (Fig EV1A), we also observed a significant increase in CHN-1 auto-Ub in the presence of UFD-2, even at the earliest time point (30 min) (Fig EV1G and H). Next, we aimed to determine what molar ratio of the two E3 triggers high CHN-1 processivity. To this end, we performed UFD-2 titrations (0.3, 0.65, and 1.3 μ M) with a fixed concentration of CHN-1 (1.3 μ M). We observed an almost twofold increase in CHN-1 auto-Ub in the presence of 0.65 μ M UFD-2, which roughly translates to one CHN-1 dimer per one UFD-2 monomer (Fig 1B). At higher UFD-2 concentrations, we did not observe any further increase in CHN-1 ubiquitylation; however, this effect could also be related to a Ub shortage in the reaction buffer, as UFD-2 robustly consumes the available Ub for its auto-Ub (Fig EV1B). Additionally, by deleting the CHN-1 TPR domain and generating CHN-1(Δ 110aa), we confirmed the involvement of the TPR domain in UFD-2 binding (Hoppe *et al*, 2004), as we did not observe an increase of CHN-1(Δ 110aa) activity by UFD-2 (Fig EV1I). Therefore, we wanted to test whether UFD-2 can regulate the processivity of

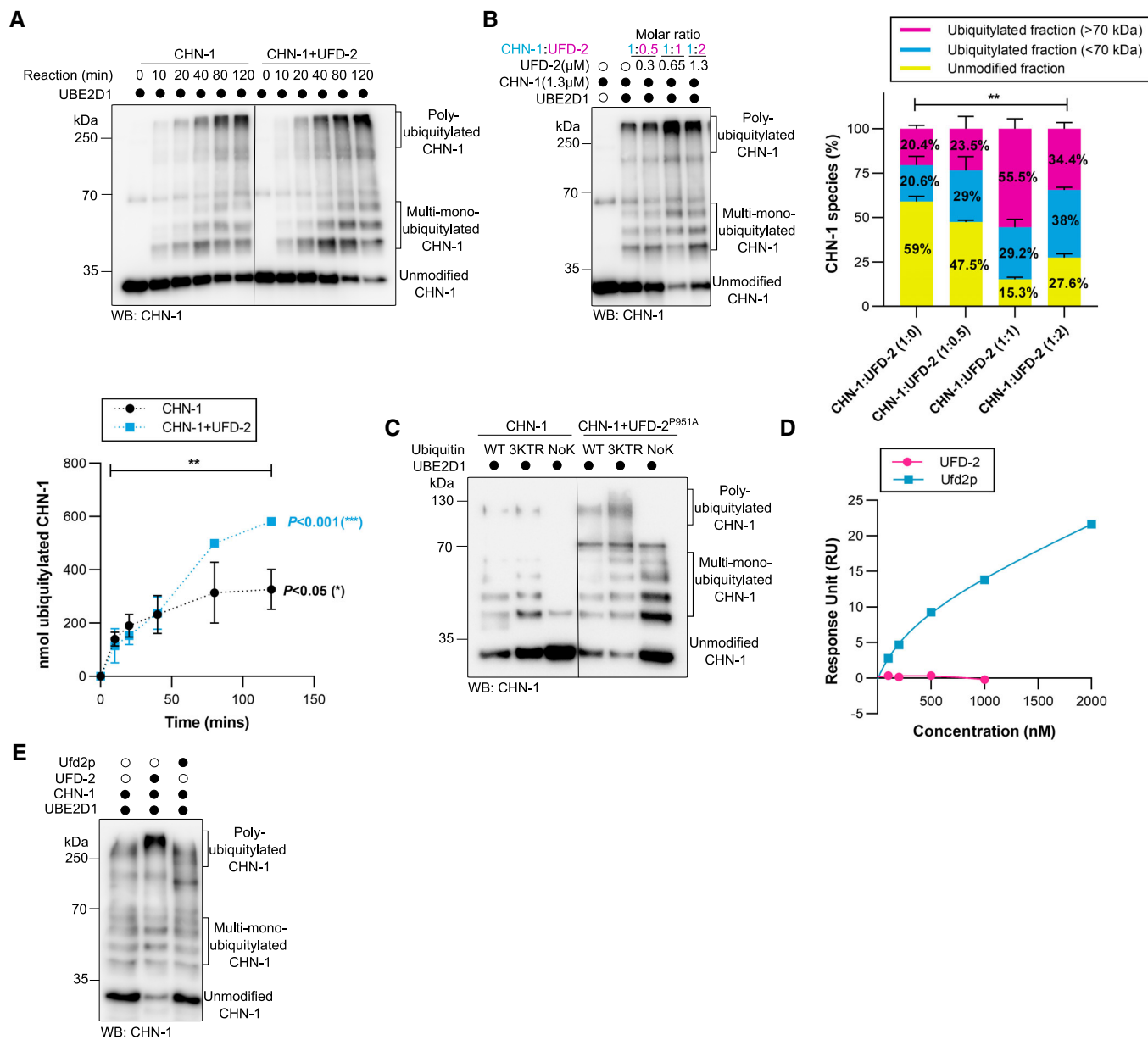


Figure 1. UFD-2 activates CHN-1.

- A** Time-dependent (0, 10, 20, 40, 80, and 120 min) CHN-1 auto-Ub was performed as indicated using Ub^{WT} and UBE2D1 E2. Protein samples were resolved via SDS-PAGE and immunoblotted with anti-CHN-1 antibodies. Below, a graph representing the nmol of ubiquitylated CHN-1 vs. time for CHN-1 alone (black) or CHN-1 + UFD-2 (cyan). Plotted data are the mean of three technical replicates. Error bars represent the standard error of measurement (SEM); statistical significance was determined using Pearson's correlation coefficients which define the statistical relation between two continuous variables [CHN-1 vs. time, CHN-1 + UFD-2 vs. time, and CHN-1 vs. CHN-1 + UFD-2 with increasing time] (* $P < 0.05$; ** $P < 0.01$; *** $P < 0.001$).
- B** CHN-1 auto-Ub was performed in the presence of UFD-2 with the increasing molar concentration as indicated. Protein samples were resolved via SDS-PAGE and immunoblotted with anti-CHN-1 antibodies. Right, signal quantification of the unmodified CHN-1 (yellow), ubiquitylated fraction < 70 kDa (cyan) and > 70 kDa (magenta), plotted as a percentage of different CHN-1 species present in the indicated condition. Plotted data are the mean from the three technical replicates. Error bars represent the SEM; statistical significance was determined using a two-way ANOVA test (** $P < 0.01$).
- C** Auto-Ub was performed as indicated using recombinant CHN-1 and UFD-2^{P951A}, UBE2D1 E2, Ub^{WT}, Ub^{NoK}, or Ub with substitutions of lysines 29, 48, and 63 to arginines (Ub^{3KTR}). Protein samples were resolved via SDS-PAGE and immunoblotted with anti-CHN-1 antibodies.
- D** Surface plasmon resonance (SPR) sensorgrams of the interaction between linear di-Ub (M1- linear from UbiQ) and *C. elegans* UFD-2 (magenta) or *S. cerevisiae* Ufd2p (cyan). Y-axis: Response unit (RU) value. X-axis: nmolar (nM) concentration of linear di-Ub.
- E** CHN-1 auto-Ub was performed as indicated in the presence of recombinant *C. elegans* UFD-2 or *S. cerevisiae* Ufd2p and UBE2D1 E2. Protein samples were resolved via SDS-PAGE and immunoblotted with anti-CHN-1 antibodies.

Data information: Representative immunoblots for at least three independent experiments are shown in the panels.

CHN-1 independent of its E3 activity. First, we found that the defect in UFD-2^{P951A} activity is due to its inability to bind an E2 enzyme (Fig EV1J). Next, we performed a CHN-1 ubiquitylation reaction in the presence of UFD-2^{P951A}. We detected substantial enhancement of both the mono- (using lysine-less Ub (UbK0)) and the poly-Ub activity of CHN-1, regardless of the type of Ub chain (wild-type Ub or variants with substitutions of lysines 29, 48, 63 to arginines (Ub3KTR) (Fig 1C). To rule out the possibility that UFD-2^{P951A} retained residual activity, we also used a UFD-2 variant (1–910 aa) lacking the entire U-box domain (909–984 aa). We confirmed that this UFD-2 deletion mutant could still stimulate CHN-1 activity (Fig EV1K). Our results suggest that UFD-2 binding to CHN-1 via its TPR domain enhances the cooperation between CHN-1 and E2s, thus resulting in more efficient auto-Ub.

Budding yeast protein Ufd2p can operate as a Ub chain elongation factor by interacting directly with Ub through its N-terminal region (Liu *et al*, 2017). Although higher eukaryotes have an ortholog of yeast Ufd2p, the Ub-interacting motif has little sequence homology (Hänzelmann *et al*, 2010; Liu *et al*, 2017), suggesting that the function of UFD-2 as an E4 is not evolutionarily conserved. To investigate whether the increased activity of the CHN-1–UFD-2 complex might stem from the elongation function of UFD-2, we tested whether UFD-2 retained its ability to interact with Ub using surface plasmon resonance (SPR) experiments. By contrast to Ufd2p, full-length UFD-2 did not bind linear Ub chains (Fig 1D). Unlike yeast Ufd2p, and perhaps to compensate for Ub binding loss, UFD-2 can induce processivity of its partner CHN-1 (Fig 1A and E). This observation suggests that UFD-2 lost its ability to directly elongate Ub chains during evolution.

UFD-2 induces a structural gain of function in CHN-1

The different conformations afforded by dynamic and flexible motifs and oligomerization are important for the functionality of various E3 ligases (Liu & Nussinov, 2011; Kamadurai *et al*, 2013; Narayan *et al*, 2015; Koliopoulos *et al*, 2016; Faull *et al*, 2019). Therefore,

we decided to analyze CHN-1 for oligomerization and conformational flexibility after binding to UFD-2. We observed a tendency of CHN-1 to form oligomers, which can be seen in the size-exclusion chromatography (SEC) as a prominent peak corresponding to its oligomeric distribution followed by a peak corresponding to the CHN-1 dimer (Fig EV2A). When we mixed CHN-1 and UFD-2 in equal molar ratios and performed SEC separation, we obtained peaks corresponding to the respective proteins without the CHN-1 oligomerization signal, suggesting a shift toward CHN-1 dimer stabilization by UFD-2 (Fig EV2A). Unfortunately, we did not detect a stable CHN-1–UFD-2 complex upon SEC separation, highlighting the dynamic and transient nature of this interaction.

To gain mechanistic insight into the role of UFD-2 binding to CHN-1, we performed hydrogen-deuterium exchange mass spectrometry (HDX-MS) of the dimerization process of both CHN-1 alone and CHN-1 in the presence of UFD-2. We detected 99 peptides with 84.2% sequence coverage of CHN-1. Some discrepancies in the profile of detected peptides between the two conditions (CHN-1 alone and CHN-1 + UFD-2) (Fig EV2B and Table EV1). In this table, peptides with missing "Frac Diff DU %" values are CHN-1 peptides that were not detected when CHN-1 was complexed with UFD-2. However, most of these were redundant with other detected peptides, except for the "NNLKMT" peptide, which extends from the 52nd to 57th residue on CHN-1 and is a linker between the pair of antiparallel alpha helices of the 2nd TPR in CHN-1. This may indicate that CHN-1 interacts with UFD-2 through this region. However, this peptide was not detected over the entire time range of the HDX-MS experiment, and therefore, its role in the CHN-1–UFD-2 complex cannot be determined. Figures 2A and EV2B depict the following model of our HDX-MS data, which detects at least three dynamic events at 10 s and 60 s. Namely: (i) the turn in the coil-coil motif (aa 145–159) is stabilized early on upon dimerization of the coil-coil domains, (ii) the TPR domain is stabilized upon recognition by UFD-2, leaving the distal helices (aa 21–40 and 92–112) exposed to the solvent. At later times, the TPR domain stabilizes against the long helix of the coil-coil domain, (iii) the U-box domain (aa 198–

Figure 2. UFD-2 stabilizes CHN-1 U-box dimer.

- A HDX-MS was used to analyze changes in the structural dynamics of residues within CHN-1 when complexed with UFD-2. The model diagram represents regions of retarded (red) and enhanced (blue) exchange in CHN-1. Right, schematics showing CHN-1 domain organization and the rate of deuterium exchange (colored box: blue, light red, medium red, and dark red) in the different domains upon interaction with UFD-2.
- B CHN-1 auto-Ub was performed as indicated using increasing molar concentrations (0.5, 1, 2, 3, 4 μM) of UBE2D1 E2 without and with a complexing equimolar concentration (1:1) of recombinant CHN-1 and UFD-2^{P951A} (1.5 μM CHN-1 with 1.5 μM of recombinant UFD-2^{P951A}). Protein samples were resolved via SDS–PAGE and immunoblotted with anti-CHN-1 antibodies. Right, a graph representing the nmol of ubiquitylated CHN-1 vs. UBE2D1 (μM) for CHN-1 alone (black) or CHN-1 + UFD-2^{P951A} (cyan). Plotted data are the mean from the three technical replicates. Error bars represent the SEM; statistical significance was determined using Pearson's correlation coefficients which define the statistical relation between two continuous variables [nmol of ubiquitylated CHN-1 vs. UBE2D1 (μM) in the presence of CHN-1 or CHN-1 + UFD-2^{P951A} and CHN-1 vs. CHN-1 + UFD-2^{P951A} with increasing UBE2D1 (μM)] (* $P < 0.05$; **** $P < 0.0001$).
- C Discharging assay of Ub-charged UBE2D1 was carried out in the presence of CHN-1 or CHN-1–UFD-2^{P951A}. The experimental sample was run together with the control with and without a reducing agent (50 mM DTT). The reaction was stopped after 30 min via the addition of Laemmli sample buffer. Proteins were resolved via SDS–PAGE and immunoblotted with anti-UBE2D1 antibodies. Below, quantification of uncharged UBE2D1 plotted as the uncharged UBE2D1 fraction vs. UBE2D1–Ub (μM). Plotted data are the mean of three technical replicates. Statistical significance was determined using Pearson's correlation coefficients which define the statistical relation between two continuous variables [UBE2D1 vs. UBE2D1–Ub (μM) in the presence of CHN-1 or CHN-1 + UFD-2^{P951A} and CHN-1 vs. CHN-1 + UFD-2^{P951A} with increasing UBE2D1–Ub (μM)] ($P < 0.05$; *** $P < 0.001$; **** $P < 0.0001$).
- D CHN-1 auto-Ub was performed as indicated in the presence of Ube2W–Ub or Ube2W–Ub^{FLAG} without and with equimolar concentration of recombinant CHN-1 and UFD-2^{P951A}. Protein samples were resolved via SDS–PAGE and immunoblotted with anti-CHN-1 antibodies. For each sample, the quantified relative signal after probing the blot using anti-CHN-1 antibodies is shown as a ratio above the respective signal. Below, a schematic of the CHN-1–Ub^{FLAG} (cyan), CHN-1–Ub (magenta), and unmodified CHN-1 signal (black) presented as the ratio and the signal fold change between CHN-1 and CHN-1–UFD-2^{P951A}.

Data information: Representative immunoblots for at least three independent experiments are shown in the panels. Source data for HDX-MS measurements are available in the Table EV1.

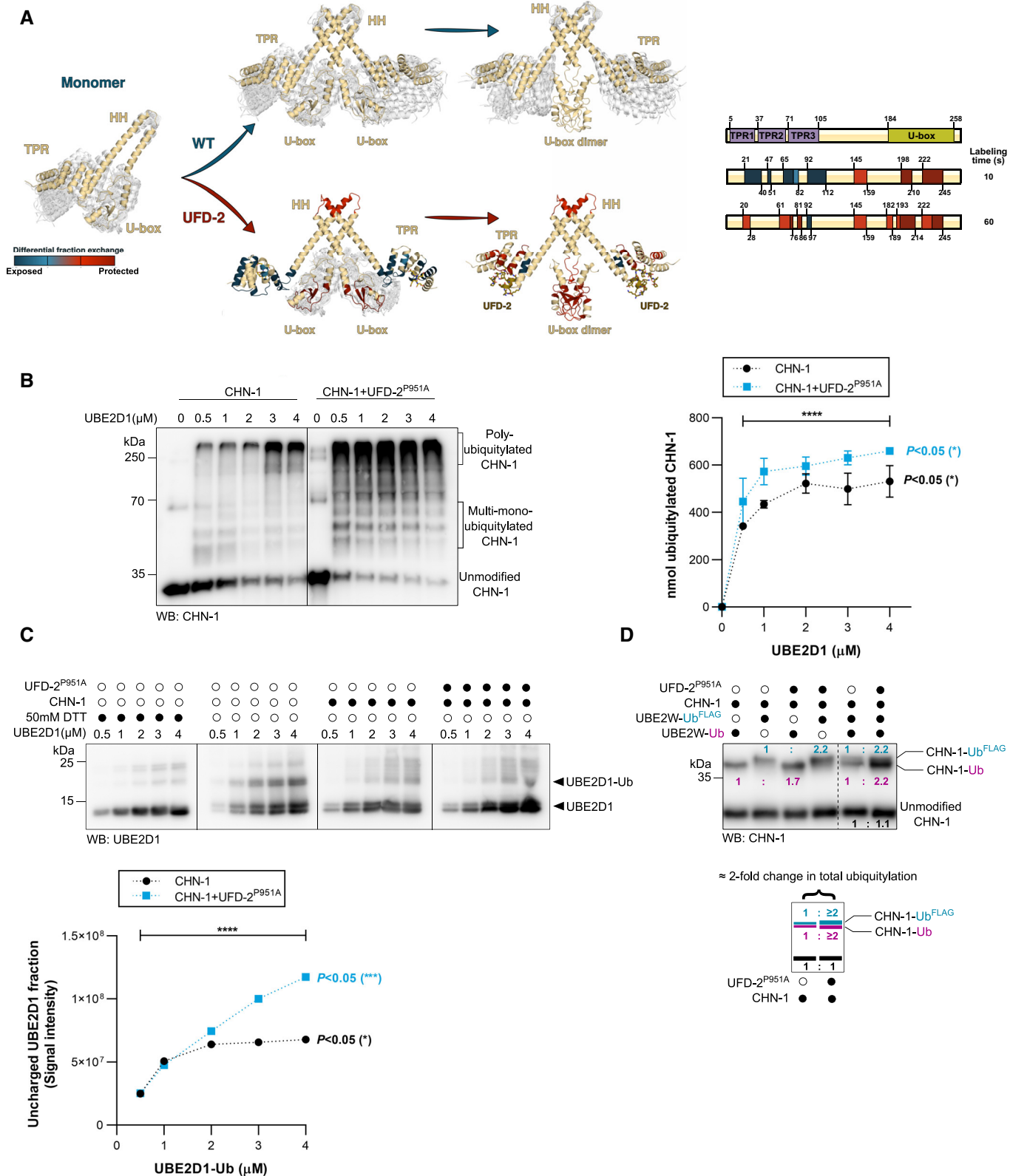


Figure 2.

245) transitions from a weak interaction with its coil-coil domain to a stable dimer on a longer time scale. Available crystal structures of CHIP homologs support our HDX-MS analysis without a chaperone (Nikolay *et al.*, 2004) and with HSP90 (Zhang *et al.*, 2005). In the absence of a TPR-binding chaperone, only the dimer domains are revealed by the crystal structure, with no resolution of either the turn in the coil-coil domain or the TPR domain. Notably, the TPR domain has only been resolved by NMR, whereas it stabilizes into its crystal form in the presence of an HSP substrate (Zhang *et al.*, 2005). Furthermore, structural analysis of murine CHIP shows that the bound TPR domain is further stabilized against the long helix of its coiled-coil domain in one of its monomers (Zhang *et al.*, 2005; Ye *et al.*, 2017). Our computational model noted that this interaction is much weaker in CHN-1, suggesting more structural dynamics in worms. Based on prediction with AlphaFold-Multimer (preprint: Evans *et al.*, 2022), we argue that, unlike CHIP (Zhang *et al.*, 2005; Ye *et al.*, 2017), CHN-1 folds into a symmetric structure. It has been shown that HSP90 negatively regulates CHIP activity (Narayan *et al.*, 2015), presumably by blocking the E2 binding site of one of the protomers (Zhang *et al.*, 2005). Thus, our finding that UFD-2 promotes CHN-1 processivity is consistent with a symmetric structure for CHN-1—in such a system, upon binding, UFD-2 stabilizes the U-box dimer with both E2 sites (Fig EV2C).

To investigate this possibility, we titrated UBE2D1 (0.5–4 μM) at a fixed concentration of CHN-1 (1.3 μM) or CHN-1 complexed with UFD-2^{P951A}, which cannot interact with UBE2D1, and conducted an auto-Ub assay. We observed that at a constant Ub concentration, increasing the E2 concentration led to increased CHN-1 activity. However, even at the highest E2 concentration (4 μM), CHN-1 processivity did not reach the same level as in the presence of inactive UFD-2^{P951A} and approximately eightfold lower E2 concentration (0.5 μM) (Fig 2B). Thus, the increased CHN-1 activity of the CHN-1–UFD-2 complex was not due to an increased local E2 concentration but rather to the enhanced processivity of the E2 enzyme bound to the CHN-1 U-box domains. To verify this hypothesis, we performed an E2-discharging assay in the presence of CHN-1 alone or after mixing with UFD-2^{P951A} to track the use of charged-E2 by CHN-1 only. We observed that in the presence of UFD-2^{P951A}, CHN-1 could discharge at least twice as much UBE2D1-Ub compared with CHN-1 alone, which becomes prominent when used 2 μM concentration of UBE2D1-Ub, which was revealed by the increasing accumulation of uncharged UBE2D1 (Figs 2C and EV2D). These results suggest that the binding of inactive UFD-2^{P951A} can stabilize the U-box dimer CHN-1 and that both domains can bind and unload E2. To further verify this possibility, we performed another auto-Ub assay with the Ube2W conjugating enzyme, which is known to maintain a strict 1:1 stoichiometry with a substrate (Christensen *et al.*, 2007; Tatham *et al.*, 2013; Vittal *et al.*, 2013) and to catalyze mono-Ub of CHIP (Scaglione *et al.*, 2011). Considering these characteristics, we added CHN-1 or CHN-1/UFD-2^{P951A} to Ub-charged Ube2W or Ub^{FLAG}-charged Ube2W and followed the ubiquitylation profile. When both charged E2 species are included in the reaction, we should observe mono-Ub of CHN-1 by Ub and Ub^{FLAG} (due to the FLAG tag, Ub molecules migrate slower on SDS–PAGE, allowing differentiation of mono-Ub from mono-Ub^{FLAG} on a single immunoblot) and a twofold increase in the level of CHN-1 ubiquitylation for the complex with UFD-2^{P951A} compared with that of CHN-1 alone. Indeed, we noted the predicted increase in CHN-1 mono-Ub with

the two Ub variants (Fig 2D), which confirms double increase in E2 enzyme capacity of CHN-1 in the presence of UFD-2. It has been previously shown that HSP70 chaperone can reduce CHIP-dependent ubiquitylation of folded substrates (Wang *et al.*, 2011; Narayan *et al.*, 2015; Kim *et al.*, 2017). To verify whether the worm ortholog of HSP70, HSP-1, affects the interaction of CHN-1 with E2, we performed another auto-Ub experiment with charged Ube2W. Indeed, the presence of HSP-1 in the reaction reduced the Ub conjugation to CHN-1 and altered the ratio of Ub to Ub^{FLAG} (Fig EV2E). The increase in the stoichiometric ratio of ubiquitylated CHN-1 in the presence of UFD-2^{P951A} suggests the existence of dimeric CHN-1 with two available U-box domains, while its HSP-1-induced decrease might suggest that HSP-1 promotes a CHN-1 conformation that limits E2 access to the U-box domains.

HSP-1 and UFD-2 modulate CHN-1 processivity by stabilizing its inactive and active conformation, respectively

The three TPR domains in CHIP act as a binding platform for C-terminal peptides of the HSP70 and HSP90 chaperones, which contain a conserved EEVD motif (Zhang *et al.*, 2005, 2015; Paul & Ghosh, 2014). As CHN-1 also binds UFD-2 via the TPR domain, we investigated whether HSP-1 or DAF-21 (the nematode HSP90 ortholog) could interfere with the interaction between CHN-1 and UFD-2. We first examined protein-protein interactions between CHN-1 and UFD-2, HSP-1, or DAF-21 using enzyme-linked immunosorbent assays (ELISAs). CHN-1 showed a higher affinity for HSP-1 and DAF-21 compared with UFD-2 (Fig EV3A). Next, we tested whether the chaperones could compete with UFD-2 for CHN-1 binding. We performed an ELISA-based titration assay to determine the dissociation of CHN-1 from immobilized UFD-2 induced by the presence of HSP-1 or DAF-21. As the concentration of chaperones increased, the CHN-1 signal decreased (increased dissociation from the complex with UFD-2), indicating that chaperones compete with UFD-2 for the CHN-1 (Fig EV3B and C). To verify the influence of HSP-1 and DAF-21 on the activity of the CHN-1–UFD-2 pair, we performed auto-Ub reactions in the presence of the chaperones. HSP-1 significantly reduced the auto-Ub activity of CHN-1 and blocked the stimulatory capacity of UFD-2 in this process (Figs 3A and EV3D). Removal of the C-terminal EEVD motif mitigated the inhibitory effect of HSP-1. By contrast, DAF-21 did not affect the UFD-2-dependent enhancement of CHN-1 activity (Fig 3A).

Next, we performed peptide mapping on peptide microarrays to pinpoint the interaction interface between the two ligases. For this, we used purified CHN-1 tagged with His::SUMO and His::SUMO alone (as a control). These proteins were incubated on two UFD-2 peptide microarrays consisting of 7- and 13-aa peptides. Signal enrichment analysis suggested that the two UFD-2 consensus sequences, EAKAELEEE and EEYDDVPE, were the predominant interactor motifs. HSP70/90 uses a similar acidic C-terminal peptide with the EEVD sequence to bind to the TPR domain of target proteins (Scheufler *et al.*, 2000; Gazda *et al.*, 2013), and the HSP-1 C-terminal EEVD peptide affected CHN-1 activity (Fig 3B). Therefore, we examined whether the identified UFD-2 peptides could also regulate CHN-1. To this end, we performed CHN-1 auto-Ub reactions in the presence of the UFD-2-derived peptides identified in the peptide microarray data. We found that only the KKEYEAKAELEEEYDDVP peptide from UFD-2 significantly stimulated CHN-1 auto-Ub

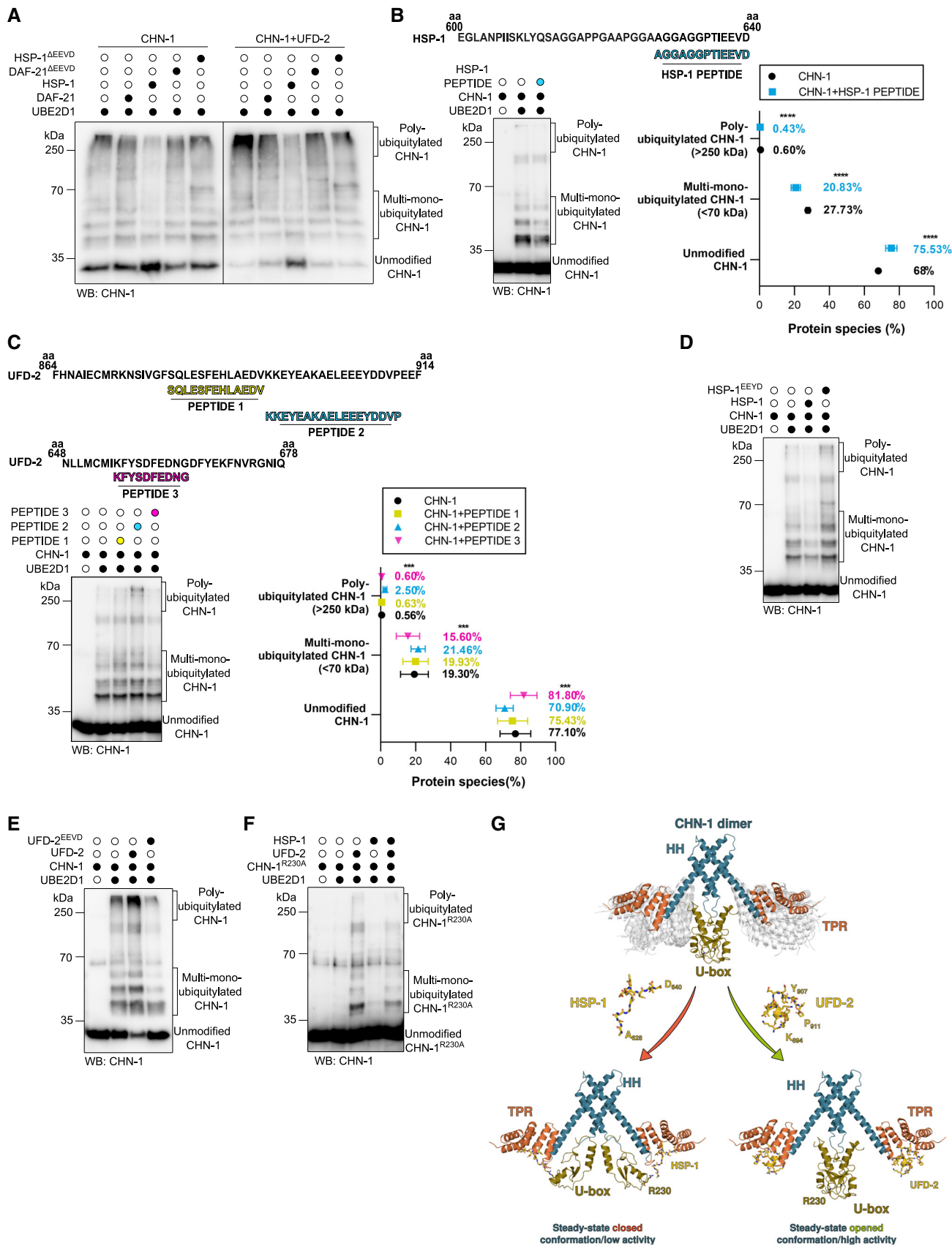


Figure 3.

Figure 3. UFD-2 stabilizes an open/active CHN-1 conformation and HSP-1 stabilizes a closed/non-active CHN-1 conformation.

- A Auto-Ub of recombinant CHN-1 using UBE2D1 E2 was performed as indicated, alone or when complexed with UFD-2, and in the presence of recombinant DAF-21, DAF-21^{ΔEEVD}, HSP-1, or HSP-1^{ΔEEVD}. Protein samples were resolved via SDS-PAGE and immunoblotted with anti-CHN-1 antibodies.
- B Top, schematics of the HSP-1 peptide sequence (cyan) aligned with the C-terminal sequence of full-length HSP-1 (amino acids 600–640) used in the ubiquitylation reaction. Auto-Ub of recombinant CHN-1 was performed as indicated in the presence of HSP-1-derived peptide and UBE2D1 E2. Protein samples were resolved via SDS-PAGE and immunoblotted with anti-CHN-1 antibodies. Right, quantification of the CHN-1 modifications (Unmodified, Multi-mono-ubiquitylated, Poly-ubiquitylated) when CHN-1 alone (black) or CHN-1 + HSP-1 peptide (cyan). Plotted data are the mean of three technical replicates. Error bars represent the SEM; statistical significance was determined using a two-way ANOVA test (**** $P < 0.0001$).
- C Top, schematics of the UFD-2 peptide sequences aligned with the C-terminal sequence of full-length UFD-2 (amino acids 864–914) for PEPTIDE 1 (yellow) and PEPTIDE 2 (cyan), and (UFD-2 amino acids 648–678) for PEPTIDE 3 (magenta) used in the ubiquitylation reaction. Below, auto-Ub of recombinant CHN-1 was performed as indicated in the presence of UFD-2-derived peptides using UBE2D1 E2. Protein samples were resolved via SDS-PAGE and immunoblotted with anti-CHN-1 antibodies. Right, quantification of the CHN-1 modifications (Unmodified, Multi-mono-ubiquitylated, Poly-ubiquitylated) when CHN-1 alone (black), CHN-1 + PEPTIDE 1 (yellow), CHN-1 + PEPTIDE 2 (cyan), or CHN-1 + PEPTIDE 3 (magenta). Plotted data are the mean of three technical replicates. Error bars represent the SEM; statistical significance was determined using a two-way ANOVA test (** $P < 0.001$).
- D Auto-Ub of recombinant CHN-1 was performed as indicated using UBE2D1 E2 in the presence of recombinant HSP-1 or HSP-1^{EEVD}. Protein samples were resolved via SDS-PAGE and immunoblotted with anti-CHN-1 antibodies.
- E Auto-Ub of recombinant CHN-1 was performed as indicated using UBE2D1 E2 in the presence of recombinant UFD-2 or UFD-2^{EEVD}. Protein samples were resolved via SDS-PAGE and immunoblotted with anti-CHN-1 antibodies.
- F CHN-1^{R230A} auto-Ub was performed as indicated using UBE2D1 E2 in the presence of recombinant UFD-2 and HSP-1. Protein samples were resolved via SDS-PAGE and immunoblotted with anti-CHN-1 antibodies.
- G Model of UFD-2 activation and HSP-1 inhibition of CHN-1. Dimeric CHN-1 with the TPR domain, U-box, and helix-turn-helix (HH) is indicated by magenta, gold, and cyan, respectively. UFD-2 and HSP-1 peptides are shown in yellow with the indicated amino acid positions in the full-length proteins.
- Data information: Representative immunoblots for at least three independent experiments are shown in the panels.

(Fig 3C). An EEVD sequence is present in this peptide, suggesting that UFD-2 can utilize an EEVD-like motif for CHN-1 binding. Furthermore, multiple sequence alignment revealed that in the EEVD motif of UFD-2, the tyrosine (Y) is evolutionarily conserved among higher eukaryotes (Fig EV3E). To define the functional role of the UFD-2 EEVD motif, we generated a chimeric recombinant HSP-1 protein carrying an N-terminal EEVD instead of EEVD and UFD-2 with the opposite change (EEVD to EEVD). Notably, we observed stimulation of CHN-1 auto-Ub by HSP-1^{EEVD}, opposite to the inhibitory effect of wild-type HSP-1 (Figs 3D and EV3F). By contrast, UFD-2^{EEVD} no longer stimulated CHN-1 activity and even mildly reduced it (Fig 3E). This observation suggests a key role for the conserved tyrosine residue at the C-terminus of UFD-2 in the binding and regulating of the CHN-1 activity switch.

Next, we assessed the contribution of specific regions of the CHN-1 TPR domain in chaperone and UFD-2 binding by generating truncation variants. We showed that the first 87 amino acids ($\Delta 87$ variant) are not responsible for the interaction with UFD-2 and HSP-1 and, therefore, are not involved in the modulation of CHN-1 processivity. By contrast, removing the subsequent eight residues ($\Delta 95$ variant) abrogated the CHN-1 poly-auto-Ub activity. Interestingly, the stimulating effect of UFD-2 was still observed, as indicated by an increase in mono-Ub CHN-1 ^{$\Delta 95$} (Fig EV3G). CHN-1 ^{$\Delta 95$} has residues that might be involved in an interaction with UFD-2, including D110 and subsequent coils and helices; thus, the CHN-1 ^{$\Delta 110$} mutant (lacking D110) does not show any gain of activity in the presence of UFD-2 (Fig EV1I). It is known that a position homologous to D110 in mouse CHIP (D135) is involved in HSP90 binding (Fig EV3H), suggesting that this residue is also important for the interaction with UFD-2 (Fig EV3I).

To understand why HSP-1 and UFD-2 peptides exhibit distinct effects on CHN-1 activity, we looked closely at the mechanism by which increased HSP90 or HSP70 concentrations reduce CHIP activity (Narayan *et al.*, 2015). HSP90 stabilizes an auto-inhibited monomer in murine CHIP (Zhang *et al.*, 2005). This state involves a salt bridge between HSP90 D501 and CHIP R273, latching the U-box

and TPR domains (Fig EV3H). This observation suggests that chaperone binding can directly restrain the U-box from participating in Ub processivity. To show that a similar mechanism is at play in inhibiting ubiquitylation by HSP-1, we mutated R230 (homologous position to R273 in CHIP) to alanine to weaken the CHN-1 U-box interaction with the HSP-1 peptide, thus abrogating its inhibitory effect. Indeed, we observed reduced inhibition of the CHN-1^{R230A}–UFD-2 complex by HSP-1 (Fig 3F). This finding is consistent with the model that HSP-1 stabilizes the autoinhibited state of CHN-1 by interacting with the TPR and U-box domains, thereby affecting its interaction with E2 enzymes (Fig 3G). On the other hand, UFD-2 can avoid interacting with R230 by, for example, forming a helix that cannot extend toward the U-box, thus inducing uncorrelated mobility of the TPR domains with respect to the U-box domains that promotes a steady-state open conformation of CHN-1 (Fig 3G), which explains maintaining its boosting effect on CHN-1^{R230A}.

UFD-2 promotes CHN-1 turnover independent of E3 activity

Our *in vitro* studies indicate that interaction with UFD-2 enhances CHN-1 auto-Ub; therefore, *in vivo* interaction with UFD-2 could promote CHN-1 turnover. To verify this hypothesis, we performed a Western blot analysis of CHN-1 and UFD-2 protein levels in young adult worms. As expected, CHN-1 abundance was significantly increased in *ufd-2(tm1380)* null allele worms. Next, we used CRISPR/Cas9 editing to generate animals expressing the catalytically inactive UFD-2P951A. Consistent with our prediction, in worms expressing UFD-2P951A, the CHN-1 protein level was significantly lower than in *ufd-2(tm1380)* animals and comparable to wild-type worms (Fig 4A). Furthermore, proteasome inhibition by MG132 stabilized CHN-1 in wild-type worms to levels similar to those in *ufd-2(tm1380)* worms (Fig 4B). Finally, in *ufd-2(tm1380)* animals, MG132 treatment did not increase the CHN-1 level further (Fig 4B). These data indicate that independent of ubiquitylation activity, UFD-2 is involved in CHN-1 turnover, presumably by promoting CHN-1 auto-Ub, which might lead to its proteasomal degradation.

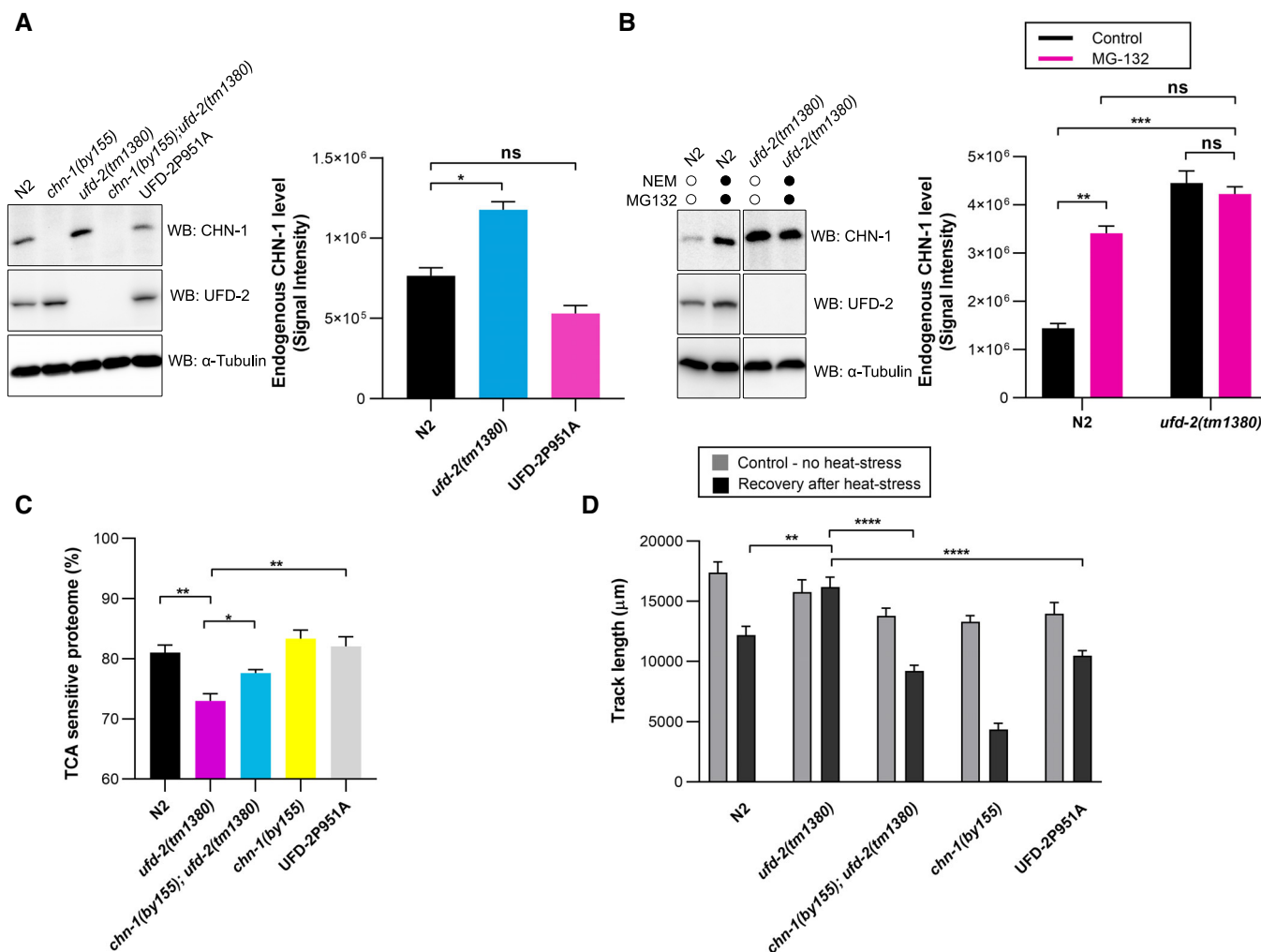


Figure 4. UFD-2 regulates CHN-1 turnover.

- A** To detect CHN-1 and UFD-2, indicated lysates of young adult worms were subjected to immunoblotting with anti-CHN-1 and anti-UFD-2 antibodies. Tubulin served as a loading control. Right, quantification of the CHN-1 signals normalized to tubulin levels and plotted as N2 (wild-type; black), *ufd-2(tm1380)* (cyan), and UFD-2P951A (magenta). Plotted data are the mean of three biological replicates. Error bars represent the SEM; statistical significance was determined using an unpaired *t*-test (* $P < 0.05$).
- B** CHN-1 protein levels were determined in the indicated lysates of young adult worms treated with a proteasome inhibitor (MG-132, 10 μ M) and DUB inhibitor (NEM, 100 mM). Tubulin served as a loading control. Right, quantification of the CHN-1 signals normalized to tubulin levels plotted as control (black), or MG-132 treated (magenta) in N2 (wild-type) and *ufd-2(tm1380)*. Plotted data are the mean of three biological replicates. Error bars represent the SEM; statistical significance was determined using an unpaired *t*-test (** $P < 0.01$; *** $P < 0.001$).
- C** Graph showing the comparison of protein solubility in the presence of 10% trichloroacetic acid (TCA) presented as TCA sensitive proteome in percentage (%) in N2 (wild-type; black), *ufd-2(tm1380)* (magenta), *chn-1(by155); ufd-2(tm1380)* (cyan), *chn-1(by155)* (yellow) and UFD-2P951A (gray) worms. Y-axis shows the percent of the entire protein sample sensitive to TCA treatment. Plotted data are the mean of three biological replicates. Error bars represent SEM; statistical significance was determined using a one-way ANOVA test (* $P < 0.05$; ** $P < 0.01$).
- D** Measurement of the mobility of the indicated young adult worms exposed to 33°C heat stress (2 h). Graph plotted as control (gray), or recovery after heat stress (black) for N2 (wild-type), *ufd-2(tm1380)*, *chn-1(by155); ufd-2(tm1380)*, *chn-1(by155)* and UFD-2P951A worms. Plotted data are the mean of three biological replicates. Error bars represent SEM; statistical significance was determined using a one-way ANOVA test (** $P < 0.01$; **** $P < 0.0001$).

This outcome might have negative consequences for proteostasis, for example, during proteotoxic stress, as it would decrease the level of CHN-1, which is an important quality control E3 ligase. Therefore, we hypothesized that *ufd-2* deletion might enhance the proteostasis capacity of the organism by reducing CHN-1 turnover. To test this possibility, we examined the worm proteome that was sensitive to trichloroacetic acid (TCA) precipitation, an established

method to assess the fraction of unfolded and aggregation-prone proteins (Cortese *et al*, 2005; Rajalingam *et al*, 2009; Depuydt *et al*, 2016). Indeed, we observed an increased fraction of stable proteins (insensitive to TCA) in the proteome of *ufd-2(tm1380)* worms compared with wild-type, and this effect was suppressed by *chn-1* deletion (*chn-1(by155); ufd-2(tm1380)*). In contrast to the *ufd-2(tm1380)* worms, animals expressing the UFD-2P951A

displayed similar levels of unstable proteins compared with wild-type worms (Fig 4C). To further explore the functional importance of CHN-1 and UFD-2 cooperation for organismal proteostasis, we measured the motility recovery rate of synchronized worms after heat stress. The results showed improved recovery in *ufd-2(tm1380)* nematodes compared with controls. As expected, this effect was suppressed in the *chn-1(by155); ufd-2(tm1380)* double mutant, while worms expressing UFD-2P951A showed similar recovery to that of control animals (Fig 4D). In summary, our results suggest that in an E3-independent manner, stimulation of CHN-1 processivity by UFD-2 can simultaneously potentiate CHN-1 auto-Ub. One possible consequence of this interaction could be a limiting effect on the proteostasis network induced by CHN-1 turnover.

The CHN-1/UFD-2 pair regulates phosphatidylcholine synthesis via AHCY-1

Based on our results, we hypothesized that CHN-1, when functioning unaided, would exhibit low poly-Ub activity, mainly catalyzing mono-Ub of its substrates. Indeed, earlier, we showed that CHN-1 alone mono-Ub the DAF-2 insulin receptor in worms (Tawo et al, 2017). We further assumed that interaction with UFD-2 would stimulate the poly-Ub activity of CHN-1, consequently leading to efficient degradation of its specific substrates. Thus, to delineate the role of CHN-1 and UFD-2 *in vivo*, we decided to identify such substrates. We searched for proteins whose levels increased after *chn-1* deletion (substrate ubiquitylation by CHN-1 would be affected directly) or *ufd-2* (CHN-1 would not be stimulated to efficiently poly-Ub its substrates). To unbiasedly define the consequences of *chn-1* and *ufd-2* deletion on the *C. elegans* proteome and to detect proteins that accumulate in the deletion mutants, we performed label-free mass spectrometry (LC-MS/MS)-based proteomics experiment. We analyzed *chn-1(by155)*, *ufd-2(tm1380)*, and *chn-1*

(*by155*); *ufd-2(tm1380)* double-mutant worms via single-shot LC-MS/MS gradients with five biological replicates. To obtain a view on the global structure of the data, we performed dimensional reduction using principal component analysis (PCA). We observed that the proteomes of the *chn-1(by155)*, *ufd-2(tm1380)*, and *chn-1(by155); ufd-2(tm1380)* mutants clustered closer together with respect to the proteomes from wild-type animals (N2 strain) (Fig EV4A). We hypothesized that potential substrates should accumulate in all mutants; therefore, we filtered the set of significantly altered proteins requiring a two-fold enrichment in all mutants versus the N2 control strain. We obtained 65 potential substrate candidates, which we visualized via hierarchical clustering (Fig EV4B and C). These potential substrates were enriched in metabolic processes, including lipid biosynthesis, as shown in Gene Ontology over-representation analysis (Fig EV4D). Among them, we identified the AHCY-1 enzyme (Figs 5A and EV4C). AHCY-1 catalyzes the reversible hydrolysis of S-adenosylhomocysteine (SAH) to homocysteine and adenosine (Palmer & Abeles, 1976, 1979). Despite the fundamental role of AHCY-1 in metabolism, its regulatory mechanisms are still enigmatic. In a yeast two-hybrid screen using a *C. elegans* cDNA library, we identified AHCY-1 as the prominent interactor of CHN-1 (Fig EV4E). We confirmed the interaction between the two proteins in worms via co-immunoprecipitation (Fig EV4F). Next, we tested whether AHCY-1 is a CHN-1 substrate by performing *in vitro* ubiquitylation assays. We confirmed that recombinant AHCY-1 is a specific substrate of CHN-1 that UFD-2 does not ubiquitylate (Fig EV4G and H). Furthermore, in the presence of UFD-2, CHN-1 poly-Ub AHCY-1 more effectively, and the level of this modification was reduced by UFD-2^{EEVD} or HSP-1 (Figs 5B, EV4G and I). The cooperation between CHN-1 and UFD-2 is also consistent with the detection of a similar increase in the AHCY-1 level in *chn-1(by155)*, *ufd-2(tm1380)*, and double-mutant worms in our proteomic analysis (Fig 5A). To further validate this observation, we monitored the endogenous AHCY-1 level via

Figure 5. The CHN-1/UFD-2 pair regulates lipid metabolism via AHCY-1.

- Boxplot analysis showing the Z-score of normalized intensities of the 50 LC-MS/MS-identified peptides from AHCY-1 detected in N2 (wild-type), *chn-1(by155)*, *ufd-2(tm1380)*, and *chn-1(by155); ufd-2(tm1380)* mutant worms. The central band of each box is the median value, and the box defines the 25th (lower) and 75th (higher) quantile. The whiskers represent the minimum and maximum values in the data, excluding outliers. A data point is considered an outlier if the distance to the median is greater than 1.5 * inter quantile range distance to the median.
- Ubiquitylation of recombinant AHCY-1 was performed as indicated. Protein samples were resolved via SDS-PAGE and immunoblotted with anti-AHCY-1 antibodies. Right, quantification of the AHCY-1 modifications (unmodified, oligo-monoubiquitylated, poly-ubiquitylated) when CHN-1 alone (black), CHN-1-UFD-2 (magenta), or CHN-1-UFD-2^{EEVD} (cyan). Plotted data are the mean of three technical replicates. Error bars represent SEM; statistical significance was determined using a two-way ANOVA test (**P* < 0.05).
- Protein level of endogenous AHCY-1 in N2 (wild-type), *chn-1(by155)*, CHN-1 OE, and *ufd-2(tm1380)* young adult worms treated with the proteasome inhibitor (MG-132, 10 μM) and DUB inhibitor (NEM, 100 mM). Protein samples were resolved via SDS-PAGE and immunoblotted with anti-AHCY-1 antibodies. Tubulin served as a loading control. Right, quantification of the modified AHCY-1 signals plotted as Ub-modified AHCY-1 species normalized to unmodified endogenous AHCY-1 signal and plotted for N2 (wild-type; black), *chn-1(by155)* (magenta), CHN-1 OE (yellow), and *ufd-2(tm1380)* (cyan). Plotted data are the mean of three biological replicates. Error bars represent SEM; statistical significance was determined using an unpaired t-test (***P* < 0.01).
- Representative images of GFP::AHCY-1 fluorescence in *chn-1(by155)*, *ufd-2(tm1380)*, and CHN-1 OE background. Scale bar = 200 μm. Below, quantification of the AHCY-1 GFP signal plotted as fluorescence intensity for GFP::AHCY-1 expressing worms (control; black), *chn-1(by155)* (magenta), *ufd-2(tm1380)* (cyan) or CHN-1 OE (yellow). Plotted data are the mean of three biological replicates. Error bars represent SEM; statistical significance was determined using a one-way ANOVA test (*****P* < 0.0001).
- Total lipid content in N2 (wild-type), *chn-1(by155)*, *ufd-2(tm1380)*, *chn-1(by155)*, *ufd-2(tm1380)*, and CHN-1 OE young adult worms grown on control (plain) and *ahcy-1(RNAi)* (lined) feeding plates. Higher fluorescence intensity indicates increased lipid levels. Plotted data are the mean of three biological replicates. Error bars indicate SEM; statistical significance was determined using a one-way ANOVA test (****P* < 0.001).
- Schematic diagram representing the core function of AHCY-1. AHCY-1 catalyzes the reversible hydrolysis of SAH (S-adenosylhomocysteine) to Hcy (homocysteine). SAH accumulation inhibits PC (phosphatidylcholine) synthesis from PE (phosphatidylethanolamine). Right, ratio of phosphatidylcholine (PC) to phosphatidylethanolamine (PE) in N2 (wild-type; black), *chn-1(by155)* (magenta), and *ufd-2(tm1380)* (cyan) young adult worms. Plotted data are the mean of three biological replicates. Error bars indicate SEM; statistical significance was determined using a one-way ANOVA test (****P* < 0.001).

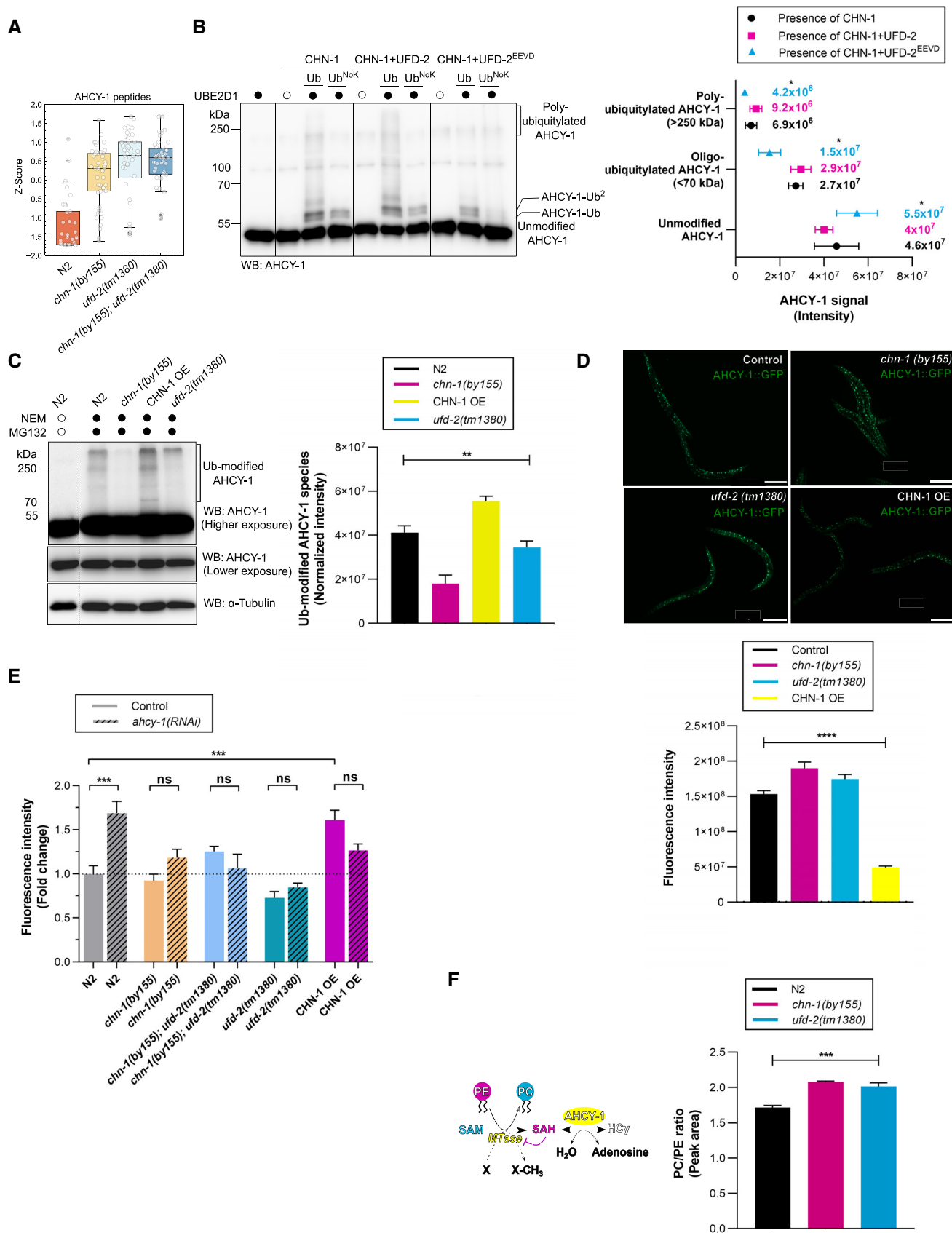


Figure 5.

Western blotting of total lysates of wild-type worms, *chn-1*(*by155*), and *ufd-2*(*tm1380*) mutant worms, as well as worms overexpressing *chn-1* (CHN-1 OE), treated with the proteasome (MG132) and deubiquitinating enzyme (DUB) (*N*-methylmaleimide, NEM) inhibitors. We did not observe any significant changes in the AHCY-1 level, which, according to our other observations, is a stable and abundant protein in *C. elegans*. However, immunoblotting with anti-AHCY-1 antibodies detected higher molecular weight smeared bands when *chn-1* was overexpressed, likely corresponding to poly-Ub AHCY-1 species (Fig 5C). Furthermore, these bands were reduced in *chn-1*(*by155*) and *ufd-2*(*tm1380*) mutant worms compared with the AHCY-1 status in wild-type animals (Fig 5C). As we did not observe a change in the stability of unmodified AHCY-1 in worm lysates, which could be related to the tendency of AHCY-1 to precipitate during sample preparation (Fig EV4K), we generated a CRISPR/Cas9 knock-in GFP-based worm line to label AHCY-1 to track its localization and abundance without compromising the integrity of the worms while maintaining its natural expression level. The GFP tag did not affect AHCY-1 functionality, as its knock-out is lethal to worms (WormBase and our observations). Next, we crossed *chn-1*(*by155*), *ufd-2*(*tm1380*), and CHN-1 OE worms with animals expressing GFP::AHCY-1. Microscopic analysis of GFP::AHCY-1 fluorescence levels revealed a significant increase in *chn-1*(*by155*) and *ufd-2*(*tm1380*) null allele worms and a decrease when CHN-1 is overexpressed (Fig 5D). Quantitative PCR analyses showed no statistically significant changes in the AHCY-1 transcript levels (Fig EV4J), suggesting that the increase in AHCY-1 levels is posttranslationally regulated by CHN-1 and UFD-2.

Elevated homocysteine levels are linked to the deregulation of lipid metabolism and increased fat accumulation, apparent after RNA interference (RNAi) depletion of AHCY-1 in worms (Vrablik et al, 2015; Visram et al, 2018). Using the lipophilic fluorophore RediStain WormDye Lipid Green to stain and quantify the fat content of *C. elegans*, we confirmed that AHCY-1 depletion increases the abundance of lipids in wild-type worms by almost 60%. Overexpression of *chn-1* caused an increase in total lipid content to a level similar to that detected in *ahcy-1* RNAi-treated worms, and this effect was not further enhanced by AHCY-1 depletion (Fig 5E). Interestingly, mutations in *chn-1* and *ufd-2* caused a reduction in the overall lipid levels and uncoupled the stimulation of lipid biogenesis induced by *ahcy-1* RNAi (Fig 5E). Synthesis of phosphatidylcholine (PC) from phosphatidylethanolamine (PE) via the *de novo* phospholipid methylation pathway requires a significant amount of *S*-adenosylmethionine (SAM) and is particularly sensitive to SAH levels (Tehlivets, 2011). Consistent with our assumption that deletion of either *chn-1* or *ufd-2* would positively affect AHCY-1 stability, leading to intensification of SAM-dependent methylation and PE to PC conversion, we noted that the ratio of PC to PE increased in *chn-1*(*by155*) and *ufd-2*(*tm1380*) worms (Fig 5F). In conclusion, our data suggest a functional role for the CHN-1–UFD-2 complex in AHCY-1-dependent lipid metabolism regulation.

Discussion

The crystal structure of murine CHIP E3 bound to an HSP90 decapeptide containing the EEVD motif revealed an asymmetric dimerization in which the two CHIP protomers adopt different

conformations. Given the limited conformational accessibility to E2 enzymes, we consider this a “closed” state, where only one of the U-box domains in the dimer is accessible for E2 binding, and the TPR domain blocks the other (Zhang et al, 2005). In agreement with a computational model of human CHIP (Ye et al, 2017), our homology modeling of the CHN-1 dimer suggested that it can take the form of both a metastable symmetric dimer (“open” state, representing unrestricted conformational accessibility to E2), in which both U-box domains can simultaneously bind E2 enzymes and an asymmetric dimer with low ubiquitylation activity. We showed that the interaction of UFD-2 with the CHN-1 TPR domain reduces its dynamics, thus liberating its U-box domains. In this steady-state open conformation, CHN-1 achieves high poly-Ub activity due to the full functionality of the U-box dimer. Consistently, we observed a twofold increase in the utilization of charged E2 by the CHN-1-UFD-2^{P951A} complex compared with that of CHN-1 alone. We also showed that not only poly-Ub but also CHN-1 mono-Ub, which is the rate-limiting step of ubiquitylation, is also enhanced upon UFD-2 binding (Petroski & Deshaies, 2005). We also found that UFD-2 is unaffected, unlike CHN-1, in the complex and that CHN-1 is not a substrate of UFD-2. We believe that CHN-1 undergoes different conformational flexibility upon binding to interaction partners, affecting its activity and providing a functional regulation layer.

The N-terminal TPR domain of CHIP has been shown to interact specifically with the C-terminal EEVD motif of HSP70 and HSP90 (Zhang et al, 2005; Xu et al, 2006; Graf et al, 2010). We discovered that UFD-2 uses a slightly modified motif, that is, EEYD, to engage the CHN-1 TPR domain. Furthermore, we demonstrated that only the presence of a UFD-2 peptide containing the EEYD sequence was sufficient to promote CHN-1 activity. By contrast, the *C. elegans* HSP70 homolog, HSP-1, negatively regulates CHN-1 and CHN-1/UFD-2 complex activity by promoting its “closed” state and preventing E2 discharge. The GHFDPVTR sequence in the U-box domain is evolutionarily conserved in CHIP homologs from different species, but its role was not previously known. Here, we showed that CHN-1 activity is negatively regulated by the interaction between positions associated with the EEVD motif of HSP-1 and the conserved R230 position in the GHFDPVTR sequence. Through direct interactions with the CHN-1 TPR and U-box domains, HSP-1 brings both regions into proximity, thereby impairing the U-box dimer. This effect depends only on the local interaction of the HSP-1 C-terminus with the U-box and not on steric hindrance induced by the entire chaperone that could limit E2 access to U-box domains. In a co-crystal structure with CHIP, HSP90 also forms hydrogen bonds (H-bonds) between T and S in its C-terminal peptide (TSRMEEVD) and the CHIP TPR domain (Zhang et al, 2005). The existence of these H-bonds between the HSP-1 peptide (GPTIEEVD) and CHN-1 is not apparent. However, the HSP-1 C-terminal sequence is rich in glycines that could more efficiently tailor the binding by forming H-bonds with the CHN-1 backbone, possibly leading to a very close interaction. It has been shown that HSP70 can interact with the CHIP TPR domain through the conserved EEVCNPIITKLYQSAGGMP sequence (in addition to the EEVD motif) (Zhang et al, 2015). However, we did not find a similar bipartite interaction between UFD-2 and CHN-1. After many attempts, we were unable to obtain a co-crystal of CHN-1 with UFD-2, and, thus, detailed insight into the organization of the complex remains enigmatic.

We observed that worm DAF-21/HSP90 has a lower affinity for CHN-1 and does not affect CHN-1 activity, unlike HSP-1/HSP70. Consistent with this observation, the C-terminal HSP70 peptide blocks CHIP activity markedly greater than the HSP90 peptide, which binds to the CHIP TPR domain weaker than the HSP70 peptide (Narayan *et al*, 2015). The K30A missense mutation in CHIP, which likely mimics HSP70 binding, also reduces CHIP activity. Furthermore, HSP70 inhibits CHIP-dependent ubiquitylation of folded substrates such as Smad1/5 (Wang *et al*, 2011), PPAR γ 2 (Kim *et al*, 2017), p53, or IRF-1 (Narayan *et al*, 2015). It is noteworthy that HSP70 can stimulate BAG-1 cochaperone ubiquitylation under experimental conditions that inhibit p53 and IRF-1 modification; however, the increase in BAG-1 modification was not accompanied by an increase in CHIP auto-Ub, an indicator of its activity. Moreover, stimulation of BAG-1 ubiquitylation was suppressed by the C-terminal peptide of HSP70 (⁶³⁴GPTIEEVD⁶⁴¹). Thus, the authors suggest that HSP70, through its direct interaction with BAG-1, may facilitate its modification by CHIP. HSP70 can also exert different effects on CHIP-dependent ubiquitylation of TP63 isoforms (a homolog of the p53 tumor suppressor), that is, it potentiates ubiquitylation of the TAp63 isoform and reduces modification of the Δ Np63 isoform (Wu *et al*, 2021). However, the authors did not present results on CHIP auto-Ub or on the competition between TP63 isoforms and HSP70 for CHIP binding, which would allow a precise determination of the effect of HSP70 on CHIP processivity in their experimental system. Two different heat-shock cognate protein 70 (HSC70, a member of the heat-shock protein 70 family) cochaperones, BAG-2 and HspBP1, limit CHIP activity (Alberti *et al*, 2004; Arndt *et al*, 2005; Dai *et al*, 2005). BAG-2 mediated inhibition is associated with reduced E2 accessibility, which is likely related to a shift favoring the CHIP “closed” state and stimulation of chaperone-assisted CFTR maturation. Moreover, CHIP can enhance the ubiquitylation of Pael-R (Parkin-associated endothelin receptor-like receptor) by Parkin E3 ligase, and this modification was inhibited by HSP70 (Imai *et al*, 2002). The *C. elegans* Parkin ortholog, PDR-1, also interacts with CHN-1, and both are expressed in neurons and body wall muscles. However, their mechanism of action and the substrates modified by the CHN-1–PDR-1 complex are obscure. In concert with our data, the above examples indicate an evolutionarily conserved role for HSP70/HSP-1 as a negative regulator of CHIP/CHN-1. We cannot exclude the possibility that posttranslational modifications of CHN-1 or the presence of specific factors that would limit the interaction of HSP-1 with the U-box domains could sustain the ability of CHN-1 to ubiquitylate chaperone-bound substrates.

To propose a non-quality-control role for the CHN-1–UFD-2 pair, we wanted to determine the protein(s) regulated by these E3s. We identified AH CY-1 as a novel substrate that undergoes ubiquitylation-dependent turnover driven by the CHN-1–UFD-2 complex. AH CY-1 is the only eukaryotic enzyme capable of hydrolyzing SAH, which is essential for SAM-dependent methylation (Cantoni, 1975). According to the results of the yeast two-hybrid screen (conducted by Hybrigenics), AH CY-1 uses its substrate-binding domain (amino acid residues 1–156) to interact with CHN-1. This finding might suggest that CHN-1 binding alone can regulate SAH processing by AH CY-1, and we intend to investigate this possibility. PC synthesis from PE via phospholipid methylation involves a significant amount of SAM and is sensitive to SAH levels; thus,

maintenance of this process requires AH CY-1 (Tehlivets, 2011). Consistent with the regulatory effect of the CHN-1–UFD-2 pair on AH CY-1, we observed an increase in PCs in worms lacking CHN-1 or UFD-2. To further understand the effect of CHN-1–UFD-2 on the SAM cycle, analysis of the levels of bound metabolites such as methionine, homocysteine, SAM, SAH, MTA, or GSH would be required. This metabolomic analysis might also help to explain the cause of the sensitivity of *chn-1*(*by155*) worms to oxidative stress (Tawo *et al*, 2017). This sensitivity might be related to the deregulation of homocysteine formation due to the impaired control of AH CY-1 as approximately 50% of the cysteine in glutathione, which plays a crucial role in cellular defence against reactive oxygen species, is derived from homocysteine (Vitvitsky *et al*, 2003). RNAi depletion of AH CY-1 increases fat accumulation in worms (Vrablik *et al*, 2015; Visram *et al*, 2018 and our results). Interestingly, we found that *chn-1* or *ufd-2* knockout inhibits the lipid biogenesis induced by *ahcy-1* RNAi. Perhaps, this effect is related to AH CY-1 stabilization in tissues that are less sensitive to RNAi, meaning that its depletion was incomplete. Recent findings support the importance of CHIP in regulating the methylation status of the cellular proteome by mediating proteasomal turnover of the SAM-dependent methyltransferases PRMT1, PRMT5, and EZH2 (Zhang *et al*, 2016; Bhuripanyo *et al*, 2018). However, further studies are necessary to delineate the involvement of the CHN-1–UFD-2 pair in modulating the cellular methylation potential. Additional CHN-1–UFD-2 substrates are likely to be present in our proteomic data set, although their confirmation requires detailed kinetic analyses.

CHN-1–UFD-2 assembly may be desirable by cells in certain contexts, such as efficiently loading a substrate for the proteasome. We observed that *in vitro*, the CHN-1–UFD-2 pair generates long Ub chains. Long Ub chains linked via Lys48 are resistant to multiple DUBs, which might promote proteasomal signaling of substrates by providing efficient targeting for degradation (Schaefer & Morgan, 2011). Furthermore, we showed that through interactions with UFD-2, CHN-1 could cooperate with various classes of E2 enzymes. We cannot exclude the possibility that in the complex, each ligase might be able to recruit different E2s, which could, in turn, enhance the generation of a mixed or branched type of Ub chains. In addition, Kuhlbrodt and coworkers suggested a link between the DUB enzyme ataxin-3 and the CHN-1–UFD-2 complex, which could allow modulation of Ub chain signaling with various functional consequences for their targets (Kuhlbrodt *et al*, 2005). While our analyses do not provide a comprehensive view of the functions of the CHN-1–UFD-2 pair *in vivo*, they establish a starting point for elucidating the details of its regulation and cellular functions.

Based on our *in vitro* data, we hypothesized that interaction of CHN-1 with UFD-2 would simultaneously increase ubiquitylation of specific CHN-1 targets and turnover of CHN-1 *in vivo*, resulting from its increased auto-Ub. Indeed, deletion of *ufd-2* in worms led to increased CHN-1 stability and protection against proteasomal degradation. Concerning the protein quality control role of CHN-1/CHIP in *C. elegans*, this stabilization would increase the proteostasis capacity. We believe that a reduction in CHN-1 processivity is probably desirable for HSP-1 as it would not lead to an imbalance between chaperone-mediated folding/maturation and degradation, inducing the latter. In summary, our data provide mechanistic insight into the distinct regulation of CHN-1 activity by HSP-1 and UFD-2.

Materials and Methods

Reagents and Tools table

Reagent/Resource	Source	Identifier
Chemicals, peptides, and Recombinant proteins		
UBE1	Boston Biochem	Cat. # E-304
UBE2D1	Boston Biochem	Cat. # E2-616
GST UbcH5a/UBE2D1	Boston Biochem	Cat. # E2-615
UBE2D2	Boston Biochem	Cat. # E2-622
UBE2D3	Boston Biochem	Cat. # E2-627
UBE2N/Uev1a	Boston Biochem	Cat. # E2-664
UBE2W	Boston Biochem	Cat. # E2-740
10X E3 Ligase Reaction Buffer	Boston Biochem	Cat. # B-71
10X Ubiquitin conjugation Reaction Buffer	Boston Biochem	Cat. # B-70
10X Energy Regeneration Solution	Boston Biochem	Cat. # B-10
Ubiquitin	Boston Biochem	Cat. # U-100H
FLAG (DYKDDDDK)-Ubiquitin	Boston Biochem	Cat. # U-120
UbNoK	Boston Biochem	Cat. # UM-NOK
Ub3KTR	Boston Biochem	Cat. # UM-3KTR
M1linked- linear ubiquitin	UbiQ	Cat. # UbiQ-L01
UBE2D1 ubiquitin charged	Boston Biochem	Cat. # E2-800
N-Ethylmaleimide (NEM)	Sigma-Aldrich	Cat. # E3876
cOmplete™, EDTA-free Protease Inhibitor Cocktail	Roche	Cat. # 11873580001
MG132	Selleckchem	Cat. # S2619
Apyrase	Sigma-Aldrich	Cat. # A2230
Alkaline Phosphatase Yellow (pNPP) Liquid Substrate	Sigma-Aldrich	Cat. # P7998
Q5 Site-Directed Mutagenesis Kit	NEB	Cat. # E0552S
4x Laemmli Sample Buffer	Bio-Rad	Cat. # 1610747
β-Mercaptoethanol	Sigma-Aldrich	Cat. # M6250
Dynabeads™ Co-Immunoprecipitation Kit	Invitrogen	Cat. # 14321D
Pierce™ Anti-DYKDDDDK Magnetic Agarose	Invitrogen	Cat. # A36797
RediStain™ WormDye Lipid Green	NemaMetrix	Cat. # DYE9439
Rapid Gold BCA Protein Assay Kit	Thermo Fisher Scientific	Cat. # A53225
IMPACT™ Kit	NEB	Cat. # E6901S
AHCY-1::6xHis	This paper	
CHN-1	This paper	
6xHis::SUMO::CHN-1	This paper	
CHN-1 ^{A110}	This paper	
CHN-1 ^{A87}	This paper	
CHN-1 ^{A95}	This paper	
CHN-1 ^{R230A}	This paper	
UFD-2	This paper	
UFD-2 ^{EEVD}	This paper	
6xHis::UFD-2	This paper	
6xHis::UFD-2 ^{P951A}	Ackermann et al (2016)	
6xHis::UFD-2 ^{AUbox}	This paper	

Reagents and Tools table (continued)

Reagent/Resource	Source	Identifier
6xHis::Ufd2p	This paper	
HSP-1::6xHis	This paper	
6xHis::DAF-21	This paper	
HSP-1 ^{ΔEEVD} ::6xHis	This paper	
6xHis::DAF-21 ^{ΔEEVD}	This paper	
HSP-1 ^{EEVD} ::6xHis	This paper	
Antibodies		
Anti-CHN-1 antibody	Tawo et al (2017)	
Anti-UFD-2 antibody	Ackermann et al (2016)	
Anti-AHCY-1 antibody	This study	
Anti-Ubiquitin antibody	Cell signaling Technology	Cat. # 3936s
Anti-Histidine antibody	Santa Cruz Biotechnology, Inc.	Cat. # SC-53073
Anti-GST antibody	Sigma-Aldrich	Cat. # G1160
Anti-UBE2D1 antibody	Biorad	Cat. # VPA00296
Bacterial Strains		
<i>E. coli</i> RNAi feeding strain	Caenorhabditis Genetics Center	HT115(DE3)
<i>E. coli</i> feeding strain	Caenorhabditis Genetics Center	OP50
Ahringer RNAi library	Source BioScience	<i>C. elegans</i> RNAi Collection (Ahringer)
Rosetta™ 2 (DE3)	Novagen	Cat. # 71400
BL21 Star™ (DE3)	Thermo Fisher Scientific	Cat. # C601003
Top10	Thermo Fisher Scientific	Cat. # C4040
Oligonucleotides		
pTYB21-MBP::Intein-UFD-2 Forward: GGTGGTTGCTCTTCCAACATGATTGAAGACGAGAAAGCAGG Reverse: GGTGGTCTGCAGTCATTATTTCTTGAATTTCTTT	This paper	
pET-6xHis::SUMO-CHN-1 ^{Δ110} Forward: ATTGAGAACGCCCTCAAAC Reverse: GCTAGCTAGACCACCAATC	This paper	
pET-6xHis::SUMO-CHN-1 ^{Δ87} Forward: TACAGTGAAGCAATAAGCTG Reverse: GCTAGCTAGACCACCAATC	This paper	
pET-6xHis::SUMO-CHN-1 ^{Δ95} Forward: TCCAAAGCGCTCTACCAT Reverse: GCTAGCTAGACCACCAATC	This paper	
pET-21a-VSV-HSP-1 ^{ΔEEVD} ::6xHis Forward: GCGGCCGCACTCGAG Reverse: TCCTCCGGCGCTCCTCC	This paper	
pET-21a-6xHis::DAF-21 ^{ΔEEVD} Forward: TAATGAGGATCCGAATTCGAG Reverse: CTCAGCTCCCTCAATCTT	This paper	
pET-6xHis::SUMO-CHN-1 ^{R230A} Forward: TCCAGTCACAGCAAACCACTTAC Reverse: TCGAAATGGCCAATTTCTT	This paper	
pTYB21-MBP::Intein-UFD-2 ^{Y907V(EEVD)} Forward: GAAGAAGAGGTTGATGATGTACCA Reverse: TGGTACATCATCAACCTTTCTT	This paper	
pET-21a-VSV-HSP-1 ^{V639Y(EEVD)} Forward: ATCGAGGAGTACGACGCGGCC	This paper	

Reagents and Tools table (continued)

Reagent/Resource	Source	Identifier
Reverse: GGCCCGCTCGTACTCCTCGAT		
Recombinant DNA		
pET28a-6xHis::Ufd2p	Liu <i>et al</i> (2017)	
pET-6xHis::SUMO::CHN-1	This paper	
pET28a-6xHis::UFD-2	This paper	
pLATE31-AHCY-1::6xHis	This paper	
pET21a-VSV::HSP-1::6xHis	This paper	
pET21a-6xHis::DAF-21	This paper	
pTYB21-MBP::Intein-UFD-2	This paper	
pET-6xHis::SUMO-CHN-1 ^{Δ110}	This paper	
pET-6xHis::SUMO-CHN-1 ^{Δ87}	This paper	
pET-6xHis::SUMO-CHN-1 ^{Δ95}	This paper	
pET-21a-VSV-HSP-1 ^{EEVD} ::6xHis	This paper	
pET-21a-VSV-HSP-1 ^{AEVD} ::6xHis	This paper	
pET-21a-6xHis::DAF-21 ^{AEVD}	This paper	
pET-6xHis::SUMO-CHN-1 ^{R230A}	This paper	
pTYB21-MBP::Intein-UFD-2 ^{Y907V(EEVD)}	This paper	
pET-21a-VSV-HSP-1 ^{V639Y(EEVD)}	This paper	
Experimental models: Organisms/Strains		
<i>C. elegans</i> : Bristol (N2) strain as wild-type	CGC	N/A
<i>C. elegans</i> : chn-1(by155)I	CGC	WormBase ID: WBVar00000641
<i>C. elegans</i> : unc-119(ed4)III; hhIs136[unc-119(+); chn-1p::chn-1::FLAG]	Tawo <i>et al</i> (2017)	N/A
<i>C. elegans</i> : ufd-2(tm1380)II	CGC	WormBase ID: WBVar00250374
<i>C. elegans</i> : chn-1(by155)I; ufd-2(tm1380) II	This paper	N/A
<i>C. elegans</i> : chn-1(by155)I; ahcy-1(syb646[ahcy-1::GFP]I)	This paper	N/A
<i>C. elegans</i> : ahcy-1(syb646[ahcy-1::GFP]I); ufd-2(tm1380)II;	This paper	N/A
<i>C. elegans</i> : unc-119(ed4)III; hhIs136[unc-119(+); chn-1p::chn-1::FLAG]; ahcy-1(syb646[ahcy-1::GFP]I)	This paper	N/A
Software and Algorithms		
Graph Pad Prism	Graph Pad Software, Inc.	www.graphpad.com
Image Lab™ Version 6.0.0 build 25	Bio-Rad Laboratories, Inc.	www.bio-rad.com/de-de/product/image-lab-software?ID=KRE6P5E8Z
ImageJ 1.53c	Wayne Rasband, NIH, USA	www.imagej.nih.gov/ij
Materials		
Nunc MaxiSorp™ flat-bottom	Thermo Fisher Scientific	Cat. # 44-2404
Hiload 16/600 Superdex S200	GE Healthcare	Cat. # GE28-9893-35

Methods and Protocols

C. elegans strains

Worms were maintained on nematode growth medium (NGM) plates seeded with OP50 *Escherichia coli* bacteria at 20°C unless otherwise stated (Brenner, 1974). The following strains were used in this study: Bristol (N2) as wild-type strain, *chn-1*(by155)I, *ufd-2*(tm1380)II, *chn-1*(by155)I; *ufd-2*(tm1380)II, *unc-119*(ed4)III;

hhIs136[*unc-119*(+), *chn-1p::chn-1::FLAG*] (Tawo *et al*, 2017). These strains were at least six times outcrossed against the wild-type strain to provide isogenic conditions. Strain generated in this study—PHX646 (*ahcy-1*(syb646[*ahcy-1::GFP*]I) and PHX792 (*ufd-2*(syb792[*ufd-2*^{P951A}]II) were generated by SunyBiotech using CRISPR services (<http://www.sunybiotech.com>). PHX646 was outcrossed 2X to N2 to generate strain WOP122. PHX792 was outcrossed 2X to N2 to generate strain WOP160.

Generation of recombinant proteins

All recombinant proteins were produced using a bacterial expression system. CHN-1 and the CHN-1 variants were expressed and purified from Rosetta™ 2 (DE3) cells. UFD-2, HSP-1, DAF-21, and their variants were expressed and purified from BL21 Star™ (DE3) cells. Truncations and point mutations in the protein constructs were introduced using the Q5 Site-Directed Mutagenesis Kit (New England Biolabs; NEB). Protein over-expression was induced using 0.4 mM IPTG at 22°C for 16 h. Respective induced cell pellets were harvested via centrifugation at 4,000 rpm for 20 min at 4°C. Cells were lysed in a lysis buffer (20 mM HEPES pH 8, NaCl 300 mM, 2 mM BME, protease inhibitor, and DNase) by sonication. After sonication, the supernatant and pellet fractions were separated via high-speed centrifugation at 14,000 rpm for 1 h at 4°C. Tagged proteins were purified from the soluble fraction of the cell lysates using appropriate Ni-NTA or GST-trap columns or chitin beads (NEB). After removing the affinity tags, affinity-purified protein fractions were subjected to gel filtration chromatography (Hiload 16/600 Superdex S200, GE Healthcare) to obtain more than 95% pure protein fractions for use in subsequent biophysical and biochemical experiments. For the *in vitro* ubiquitylation reactions, we first generated a pTYB21-UFD-2 expression vector and purified tagless UFD-2 fraction using the intein cleavage site as per the manufacturer's protocol (NEB). The lysis buffer used for purifying this variant contained HEPES 20 mM, TritonX 0.1%, 5% glycerol, 500 mM NaCl, pH 8.0. To generate tagless CHN-1 and His-tagged CHN-1, we affinity-purified the proteins using Ni-NTA columns. Furthermore, His-SUMO tag were cleaved using SUMO protease treatment (16 h) at 4°C, and untagged CHN-1 dimeric fraction was purified via SEC.

Peptide microarray for protein-peptide interaction studies

This assay was performed by PEPperPRINT GmbH (<https://www.pepperprint.com/>). Briefly, the UFD-2 sequences were elongated with neutral GSGSGG linkers on the C- and N-termini to avoid truncated peptides and translated into 7 and 13 amino acid peptides with overlaps of 6 and 12 amino acids. The resulting UFD-2 peptide microarrays (containing 1,986 different peptides) were printed in duplicate and incubated with recombinant 6xHis::SUMO::CHN-1 for 16 h at 4°C. After washing, the microarrays were incubated with mouse anti-6x-His Epitope Tag DyLight680 secondary antibodies to detect bound 6XHis::SUMO::CHN-1.

Ubiquitylation assays

In vitro assays were performed according to an earlier protocol (Hellerschmied *et al.*, 2018). The reactions were run at 30°C for 90 min using 60 μM ubiquitin and its variants (Boston Biochem) in the presence of 100 nM E1 (UBE1, Boston Biochem), 0.6 μM E2 (Boston Biochem), E3 ligase (CHN-1 and variants or UFD-2 and variants), E3 ligase reaction buffer (Boston Biochem), and Energy Regeneration Solution (Boston Biochem). For performing the *in vitro* reaction in the presence of both the CHN-1 and UFD-2 or His-tagged UFD-2^{P951A}, proteins were first preincubated at 16°C for 30 min in the presence of E3 ligase reaction buffer. After that, the remaining reagents were added for the ubiquitylation reaction and incubated at 30°C for the indicated time. For substrate

ubiquitylation, *C. elegans* AHY-1 was added as the substrate along with the other reagents and mixed with preincubated CHN-1 or pre-incubated CHN-1/UFD-2 and incubated at 30°C for 90 min. For performing the *in vitro* reaction in the presence of a chaperone, *C. elegans* 1 μM His-tagged HSP-1, His-tagged DAF-21, or other variants were preincubated with CHN-1 or CHN-1/UFD-2 at 16°C for 30 min in the presence of 1× E3 ligase reaction buffer. After that, the remaining reagents were added for the reaction and incubated at 30°C for 90 min. Reaction stopped by adding Laemmli sample buffer (Bio-Rad), including β-mercaptoethanol (Sigma-Aldrich), and incubated at 95°C for 5 min. Samples were run in 12% SDS-PAGE gels and blotted with an antibody against the protein of interest.

E2 discharging assays

E2 discharging experimental protocol was designed based on a modified method from Page *et al.*, 2012. Discharging of increasing molar concentration of charged UBE2D1 (UBE2D1-Ub, Boston Biochem) was performed at 30°C for 40 min in ubiquitin conjugation reaction buffer (Boston Biochem, Cat#B-70). Similarly, a time-dependent assay was performed using 3.3 μM UBE2D1-Ub at 30°C for different time points (5, 10, 20, 30 min) with equimolar concentrations (1 μM) of CHN-1, His-tagged UFD-2^{P951A} and His-tagged HSP-1. The reaction was stopped by the addition of Laemmli sample buffer (Bio-Rad). As a control experiment to check the total UBE2D1 used in the reaction, the charged UBE2D1 were treated with 50 mM DTT and boiled the sample at 90°C for 5 min to obtain the total uncharged E2. Samples were run in a 15% SDS-PAGE gel. For detecting the available UBE2D1-Ub in each condition, Western blotting was performed using an anti-ubiquitin or anti-UBE2D1 antibody. Normalized chemiluminescence intensity was obtained after maximum background subtraction from each lane. The discharging capacity at a specific condition was analyzed by detecting the band intensity of the uncharged fraction of UBE2D1 while probing with an anti-UBE2D1 antibody or available charged UBE2D1 while probing with an anti-ubiquitin antibody at the end of the reaction.

Generation of ubiquitin-charged GST-tagged UbCh5a/UBE2D1

1.25 μM E2 GST::UbCh5a/UBE2D1 (Boston Biochem) was charged using 58 μM ubiquitin (Boston Biochem), 0.25 μM E1 (UBE1, Boston Biochem), ATP and ubiquitin-conjugating buffer (Boston Biochem), and incubated at 30°C for 30 min. Charging reaction was stopped by adding 5 mM Ayrase (Sigma-Aldrich). The reaction mix was used as a source of UBE2D1^{GST}-Ub.

E3-ubiquitin stoichiometry analysis using UBE2W ubiquitylation assay

0.6 μM E2 UBE2W (Boston Biochem) was charged using 60 μM ubiquitin (Boston Biochem) or 60 μM FLAG-Ubiquitin (Boston Biochem) in the presence of ATP, ubiquitin-conjugating buffer (Boston Biochem) and incubated at 30°C for 30 min. After that, the conjugation reaction was stopped by adding 5 mM Ayrase (Sigma-Aldrich). Then, reaction mix containing UBE2W-Ub or UBE2W-Ub^{FLAG} was used in a discharging assay bin at 30°C for 40 min. The reaction was stopped by the addition of Laemmli sample buffer (Bio-Rad) including β-mercaptoethanol (Sigma-Aldrich), and boiled

for 5 min. Samples were run in 12% SDS–PAGE gels and blotted with an antibody against the protein of interest.

Western blotting and quantification

Protein samples in SDS-loading dye (reducing/non-reducing) were run in 12 or 15% acrylamide gels using running buffer (25 mM Tris, 190 mM glycine, 0.1% SDS) at 120 volts (constant). The wet transfer was made at a constant 200 mA for 2 h at room temperature using transfer buffer (25 mM Tris, 190 mM glycine, 10% methanol, pH 8.3). Blots were blocked with 5% skimmed milk in TBST (50 mM Tris, 150 mM NaCl, 0.1% Tween 20, pH 7.5) for 1 h at room temperature and incubated overnight with primary antibody prepared in 5% skimmed milk in TBST at 4°C. The blots were then washed three times with TBST for 10 min. Finally, the blots were incubated with secondary antibodies prepared in 5% skimmed milk in TBST for 1 h at room temperature. Imaging was performed using a ChemiDoc™ Imaging System (Bio-Rad). All antibodies used in this study are listed in the resource table. Image Lab™ (version 6.0.0 build 25) software was used for quantification. After probing with a particular antibody, first, the lane marked the bands that appeared were marked in high sensitivity mode and quantified. Normalized chemiluminescence intensities were determined after maximum background subtraction from each lane. The graphs were plotted using GraphPad Prism 9.

Enzyme-linked immunosorbent assay (ELISA)

2 µg/ml of UFD-2, His-tagged DAF-21, and His-tagged HSP-1 in coating buffer (100 mM NaHCO₃, 32 mM Na₂CO₃, pH 9.2) were immobilized on Nunc-Immuno plates for ELISA (Thermo Fisher Scientific) overnight at 4°C. Blocking was performed with 2% BSA for 1 h at 25°C, followed by washing with TBST (0.1% Tween 20). After incubation with increasing CHN-1 concentrations for 1 h at 16°C, unbound CHN-1 was washed away by subsequent TBST washing steps. Interacting proteins were detected using an antibody against CHN-1 (1:5,000 dilution, overnight 4°C), followed by TBST washing and the addition of an HRP-conjugated secondary antibody. After the final wash, 100 µl of pNPP substrate (Alkaline Phosphatase Yellow, Sigma-Aldrich) was added in the dark. After 15 min, the reaction was stopped by adding 50 µl of 3 M NaOH, and the absorbance was measured at 450 nm.

Microscopy of worms

Day 0 adult worms maintained at 20°C were immobilized with tetramisole and immediately imaged using Nikon SMZ25 microscope. Data analysis: Image processing was performed with ImageJ (Fiji) using Binary Mask and Particle Analysis Procedure with background signal subtraction.

qPCR

RNA extraction, genomic DNA digestion at the young adult (adult day 0–1) stage was performed as described in Ly et al, 2015, with the exception that min. A total of 100 worms were used instead of a single worm per sample as in the publication, cDNA synthesis was performed using the Maxima H Minus cDNA synthesis kit (Thermo Fisher). RT-PCR was performed with SG qPCR Master Mix (EURx), according to the manufacturer's protocol. Equipment used—Light Cycler 96. Data analyzed as the ratio between CT candidate gene (*ahcy-1*) averaged from 3 replicates/CT ref (actin coding gene *act-1* as a reference).

Modeling and molecular dynamics

CHN-1 model was generated by homology modeling using the SWISS-MODEL web server (Waterhouse et al, 2018) with PDB ID 2F42 and 2C2L as the templates. The primary sequence of peptides used for docking on the CHN-1 dimer model was 628–640 HSP-1 (P09446) and 894–911 UFD-2 (Q09349). The protein and peptide complex structures were subjected to an energy minimization strategy using pmem.cuda (Goetz et al, 2012; Salomon-Ferrer et al, 2013) from the AMBER18 package (Case et al, 2018). tLeap binary (part of AMBER18) was used for solvating the structures in an octahedral TIP3P water box with 15 Å distance from the structure surface to the box edges; closeness parameter was set to 0.75 Å. The system was neutralized and solvated in a solution of 150 mM NaCl. Simulations were carried out by equilibrating the system for 1 ns (NPT) at 1 atm in 300K, followed by 10 ns NPT for nonbonded interaction using the AMBER ff14SB force field (Maier et al, 2015). The particle mesh Ewald (PME) method was used to treat the long-range electrostatic interactions; hydrogen bonds were constrained using SHAKE algorithm and integration time-step at 2 fs. (Ryckaert et al, 1977).

Hydrogen deuterium exchange mass spectrometry (HDX-MS)

Prior to HDX-MS reactions, a complex of CHN-1 (3 mg/ml) and His-tagged UFD-2 (2 mg/ml) was formed by mixing the proteins in a 1:1 molar ratio followed by incubation at 25°C for 30 min. HDX-MS of CHN-1 and CHN-1 in complex with UFD-2 were performed at five time points during the incubation with deuterium (10 s, 1 min, 5 min, 25 min, and 2 h) in triplicate. 5 µl aliquots of proteins were added to 45 µl of deuterated buffer (10 mM HEPES, 150 mM NaCl in 99.99% D₂O, pH = 8.0) at room temperature. The exchange reaction was quenched by moving the exchange aliquots to precooled tubes (on ice) containing 10 µl of quenching buffer (2 M glycine, 4 M guanidine hydrochloride, 100 mM TCEP in 99.99% D₂O, pH 2.3). After quenching, samples were frozen immediately in liquid nitrogen and kept at -80°C until mass spectrometry measurement. Samples were thawed directly before measurement and injected manually onto the nano ACQUITY UPLC system equipped with HDX-MS Manager (Waters). Proteins were digested on 2.1 mm × 20 mm columns with immobilized Nepenthesin-2 (AffiPro), for 1.5 min at 20°C and eluted with 0.07% formic acid in water at a flow rate of 200 µl/min. Digested peptides were passed directly to the ACQUITY BEH C18 VanGuard pre-column from which they were eluted onto the reversed-phase ACQUITY UPLC BEH C18 column (Waters) using a 6–40% gradient of acetonitrile in 0.01% of formic acid at a flow rate of 90 µl/min at 0.5°C. Samples were measured on the SYNAPT-G2 HDX-MS instrument (Waters) in IMS mode. The instrument parameters for MS detection were as follows: ESI—positive mode; capillary voltage—3 kV; sampling cone voltage—35 V; extraction cone voltage—3 V; source temperature—80°C; desolvation temperature—175°C; and desolvation gas flow 800 l/h. The CHN-1 peptide list was obtained using non-deuterated protein samples, processed as described above for HDX experiments, and measured in Mse mode. Peptides were identified using ProteinLynx Global Server Software (Waters). The HDX-MS experiment was analyzed using DynamX 3.0 (Waters) software. The PLGS peptide list was filtered by minimum intensity criteria—3000 and minimal product per amino acid—0.3. All MS spectra were inspected manually. Final data analysis was carried out using the

in-house HaDeX software (Puchala *et al*, 2020). Differential deuterium exchange of residues was mapped to the model of CHN-1 generated using the 2C2L CHIP structure in the SWISS-MODEL Web server (<https://swissmodel.expasy.org/>). The uncertainty measurement was calculated using the uncertainty transfer law consistent with ISO standards and community guidelines.

The exact process is described in our documentation: <https://hadexversum.github.io/HaDeX/articles/datafiles.html>.

Surface plasmon resonance (SPR)

SPR-based interaction analysis was carried out at 25°C on a Biacore S200 instrument (GE Healthcare). Recombinant purified His-tagged UFD-2 and His-tagged Ufd2p proteins were immobilized on NTA Biacore sensor Chips (Series S) at 20 µg/ml. Single-cycle kinetics studies were performed by passing increasing concentrations (0, 100, 200, 500, 1,000, and 2,000 nM) of analyte M1 diUb conjugates (UbiQ) in SPR buffer (10 mM HEPES, 150 mM NaCl, 0.05% Tween 20, 0.1% BSA, 50 µM EDTA, pH 8.0). The runs for both proteins were carried out under identical conditions. All injections were compiled in the same sensorgram with the response unit (RU) on Y-axis versus time (sec) on the X-axis.

Preparation of *C. elegans* lysates and co-immunoprecipitation

Worms were grown at 20°C. For protein extraction, worms were collected in M9 buffer and lysed using a lysis buffer (50 mM KCl, 10 mM Tris-HCl pH 8.2, 2.5 mM MgCl₂, 0.07% NP-40, 0.7% Tween-20, 0.1% gelatine) with protease inhibitor (Roche) and in the presence of DUB inhibitor, NEM (Sigma-Aldrich). First, worms in lysis buffer were snap-frozen in liquid nitrogen. Next, the frozen samples were sonicated (40% amplitude, 5 cycles of 30 s pulses at 30 s intervals, Vibra-Cell™) on ice. Samples were centrifuged at 13,000 rpm for 15 min and the supernatants were collected. For co-immunoprecipitation, anti-DYKDDDDK (FLAG tag) magnetic beads (Anti-DYKDDDDK Magnetic Agarose, Pierce) were used. 50 µl of anti-DYKDDDDK magnetic beads slurry were used for 200 µl of worm lysate. Lysate of CHN-1::FLAG-expressing worms was used as the experimental sample and wild-type (N2) worms were used as a negative control. Worm lysates were incubated with equilibrated magnetic beads at 4°C for 1 and 2 h for UFD-2 and AHCY-1 pull down, respectively. After the desired incubations, the beads were washed three times using washing buffer (PBS with 100 mM NaCl). Samples were eluted via the addition of Laemmli sample buffer (Bio-Rad) containing β-mercaptoethanol (Sigma-Aldrich), and boiled for 5 min.

RNA interference (RNAi)

RNAi was performed using the standard RNAi feeding method and RNAi clones (Kamath & Ahringer, 2003). NGM plates supplemented with 1 mM IPTG and 25 µg/µl carbenicillin were seeded with HT115 *E. coli* expressing double-stranded RNA (dsRNA) against the gene of interest or, as a control, bacteria with the empty vector were used. Worms were placed on freshly prepared RNAi plates as age-synchronized L1 larvae.

TCA precipitation

Approximately 1,000 young adult worms were broken by sonication in 50% Tris-sodium dodecyl sulfate buffer (25 mM Tris, 250 mM NaCl, 5% sodium dodecyl sulfate, pH 7.4), and the debris was

pelleted by centrifugation for 5 min at 20,000 rcf. To precipitate proteins in the supernatant, trichloroacetic acid (TCA, final concentration 9.3%) was added to the supernatant and incubated at room temperature for 1 h. The supernatant was removed, leaving the protein pellet intact. Pellet was washed twice with 200 µl of cold acetone and centrifuged at 14,000 rpm for 5 min. Next, the pellet was dried by placing the tube in a 95°C heat block for 5–10 min to evaporate the acetone. The protein precipitate (TCA-insoluble fraction) was dissolved in 150 µl of 350 mM NaOH for 1 h at room temperature. Total protein concentration was determined using the Rapid Gold BCA Protein Assay (Thermo Scientific).

Heat stress recovery

Approximately 50 young adult worms were washed from NGM plates and rinsed three times with M9 buffer. The worms were further suspended in a 1 ml M9 buffer. The worms to be heat stressed were incubated at 33°C for 60 min, whereas the control animals were incubated at 20°C for 60 min. Next, worm movement was recorded for 2 min using the WormLab system (MBF Bioscience). The frame rate, exposure time, and gain were set to 7.5 frames per second, 0.0031 s, and 1, respectively. The distance the worms travelled before and after heat stress was analyzed using the WormLab software (MBF Bioscience).

Proteomics

For proteomic analysis, the following young adult strains were utilized: N2, *ufd-2(tm1380)*, *chn-1(by155)* and *ufd-2(tm1380); chn-1(by155)*. Protein digestion: 4% SDS in 100 mM HEPES pH = 8.5 was used for lysis, and the protein concentrations were determined. 50 µg of protein was subjected to tryptic digestion. Proteins were reduced (10 mM TCEP) and alkylated (20 mM CAA) in the dark for 45 min at 45°C. Samples were subjected to SP3-based digestion (Hughes *et al*, 2014). Washed SP3 beads (SP3 beads (Sera-Magcan) Magnetic Carboxylate Modified Particles (Hydrophobic), and Seracan (TM) Magnetic Carboxylate Modified Particles (Hydrophilic)) were mixed equally, and 3 µl of beads were added to each sample. Acetonitrile was added to a final concentration of 50%, and the samples were washed twice using 70% ethanol (200 µl) on an in-house-made magnet. After an additional acetonitrile wash (200 µl), 5 µl of digestion solution (10 mM HEPES pH 8.5 containing 0.5 µg Trypsin (Sigma-Aldrich) and 0.5 µg LysC (Wako) was added to each sample and incubated overnight at 37°C. Peptides were cleaned on a magnet using 2 × 200 µl acetonitrile washes and eluted in 10 µl of 5% DMSO in an ultrasonic bath for 10 min. Formic acid and acetonitrile were added to final concentrations of 2.5% and 2%, respectively. Samples were frozen until LC-MS/MS analysis. Liquid chromatography and mass spectrometry: LC-MS/MS instrumentation consisted of a nLC 1200 coupled to a nanoelectrospray source to a QExactive HF-x (Thermo Fisher Scientific) mass spectrometer. Peptide separation was performed on an in-house-packed column (75 µm inner diameter, 360 µm outer diameter), and the column temperature was maintained at 50°C using a column oven (PRSO-V2). The LC buffer system consisted out of 0.1% formic acid (A) and 0.1% formic acid in 80% acetonitrile (B). Peptides were separated using a 90 min gradient applying a linear gradient for 70 min from 7 to 29 % B and then ramped to 65% B within 10 min, followed by a linear increase to 95% B within 5 min. 95% B was held for 5 min. Before each run, the column was re-equilibrated to

0% B. The mass spectrometer operated in a data-dependent acquisition mode targeting the top 22 peaks for collision-induced fragmentation and MS2 spectra acquisition. MS1 spectra were acquired in a scan range from 350 to 1,650 m/z allowing a maximum injection time of 20 ms for an AGC target of $3e6$. Spectra were acquired at a resolution of 60,000 (at 200 m/z). Ions were isolated in an isolation window of 1.3 m/z using an AGC target of $1e6$ and a maximum injection time of 22 ms. Spectra were acquired at a resolution of 15,000. The scan range for the MS2 spectra was set to 200–2,000 m/z . The normalized collision energy was 28. Dynamic exclusion was set to 20 s. Data analysis: Acquired raw files were correlated to the Uniprot reference *C. elegans* proteome using MaxQuant (1.5.3.8) (Cox & Mann, 2008) and the implemented Andromeda search engine (Cox et al, 2011). Label-free quantification and matching between runs were enabled using default settings. Carbamidomethylation of cysteine residues was set as a fixed modification. Oxidation of methionine residues and acetylation of protein N-termini were defined as variable modifications. The false discovery rate (FDR) was controlled using the implemented revert algorithm to 1% at the protein and the peptide-spectrum match (PSM). To identify significantly changed proteins, we performed a one-way analysis of variance (ANOVA), correcting for multiple testing using a permutation-based approach (FDR < 0.05, number of permutations: 500).

Lipidomics

The following young adult strains were utilized for lipidomic analysis: N2 (wild-type), *ufd-2(tm1380)*, and *chn-1(by155)*. Lipid extraction: Lipids from a homogenized sample comprising 15 000 worms were extracted using the Folch method as follows: 200 μ l of methanol was added to each sample, followed by 10 s of vortexing. Next, 500 μ l of chloroform was added, followed by 10 s vortexing. This was followed by the addition of 200 μ l of water to each sample to induce phase separation, followed by vortexing for 20 s. The samples were then kept in the cold for 10 min and centrifuged at 14,500 rpm for the next 10 min. The bottom layer was then pipetted out, and the solvent was dried under a stream of nitrogen. The lipid extract was reconstituted in 200 μ l of 1:1 isopropanol:methanol solution before LC-MS analysis. LC-MS analysis: LC-MS analysis was performed as previously described (Alseikh et al, 2021). Briefly, lipid extracts were separated on a Kinetex C18 2.1 \times 100 mm, 2.6 μ m column (Phenomenex, Aschaffenburg, DE). Separation was achieved via gradient elution in a binary solvent, Vanquish UHPLC (Thermo Scientific, Bremen, DE). Mobile Phase A consisted of ACN:H₂O (60:40), while mobile phase B consisted of IPA:ACN (90:10). For positive ionization, the mobile phases were modified with 10 mM ammonium formate and 0.1% formic acid, while for the negative ionization mode, the mobile phases were modified with 5 mM ammonium acetate and 0.1% acetic acid. A flow rate of 260 μ l/min was used for separation, and the column and sample tray were held constant at 30°C and 4°C, respectively. 2 μ l of each sample was injected onto the LC column. MS Instrumentation: MS analysis was performed on a Q-Exactive Plus Mass Spectrometer (Thermo Scientific, Bremen, DE) equipped with a heated electrospray ionization probe. In both the positive and the negative ionization modes, the S-Lens RF level was set to 65, and the capillary temperature was set to 320°C, and the sheath gas flow was set to 30 units and the auxiliary gas was set to five units. The spray voltage was set to 3.5 kV in the negative ionization mode and

4.5 kV in the positive ionization mode. In both modes, full scan mass spectra (scan range m/z 100–1,500, R = 35K) were acquired along with data-dependent (DDA) MS/MS spectra of the five most abundant ions. DDA MS/MS spectra were acquired using normalized collision energies of 30, 40, and 50 units (R = 17.5K and an isolation width = 1 m/z). The instrument was controlled using Xcalibur (version 4.0). Data analysis and lipid annotation: Progenesis Q1, version 2.0 (Non-Linear Dynamics, A Waters Company, Newcastle upon Tyne, UK) was used for peak picking and chromatographic alignment of all samples, with a pooled sample used as a reference. Lipids were annotated using the Progenesis Metascope Basic Lipids the LipidBlast databases with consideration made only of compounds that had MS/MS data. In both databases, the precursor ion tolerance was set to 10 ppm, and the fragmentation ion tolerance was set to 15 ppm. Putative lipid identifications were based on manual curation of database matches with fragmentation scores > 10%.

Fluorescent labeling of lipids in *C. elegans*

Lipid content in young adult worms was determined by RediStain WormDye Lipid Green (NemaMetrix) staining according to the manufacturer's protocol (incubating worms with the reagent for 30 min at room temperature with shaking). Working dye concentration: 1 μ l of dye/200 μ l of M9 buffer. Worms were protected from light, and several washes in M9 buffer were performed after staining. Subsequently, after immobilization of the worms with tetramisole, imaging was performed on a Nikon SMZ25 microscope. Data analysis: Image processing was performed with ImageJ (Fiji) using Binary Mask and Particle Analysis Procedure with background signal subtraction.

Yeast two-hybrid screening

Yeast two-hybrid screening was performed by the Hybrigenics Services (<http://www.hybrigenics-services.com>). The coding sequence for *C. elegans* CHN-1 (NM_059380.5, aa 1–266) was PCR-amplified and cloned into pB27 as a C-terminal fusion to LexA (LexA-CHN-1). The construct was checked by sequencing the entire insert and used as a bait to screen a random-primed *C. elegans* mixed-stage cDNA library constructed into pP6. pB27 and pP6 were derived from the original pBTM116 (Vojtek & Hollenberg, 1995) and pGADGH (Bartel et al, 1993) plasmids, respectively. A total of 61 million clones (sixfold the complexity of the library) were screened using a mating approach with YHGX13 (Y187 *ade2-101::loxP-kanMX-loxP*, *mat α*) and L40Gal4 (*mata*) yeast strains as previously described (Fromont-Racine et al, 1997). 202 His⁺ colonies were selected on a medium lacking tryptophan, leucine, and histidine and supplemented with 50 mM 3-aminotriazole to prevent bait autoactivation. The prey fragments of the positive clones were amplified by PCR and sequenced at their 5' and 3' junctions. The resulting sequences were used to identify the corresponding interacting proteins in the GenBank database (NCBI) using a fully automated procedure. A confidence score (PBS, Predicted Biological Score) was attributed to each interaction as previously described (Formstecher et al, 2005). The PBS relies on two different levels of analysis. First, a local score considers the redundancy and independence of prey fragments and the distribution of reading frames and stop codons in overlapping fragments. Second, a global score considers the interactions found in all of the screens performed by

the Hybrigenics Services using the same library. This global score represents the probability of interaction being nonspecific. The scores were divided into four categories for practical use, from A (highest confidence) to D (lowest confidence). A fifth category (E) flags explicit interactions involving highly connected prey domains previously found several times in screens performed on libraries derived from the same organism.

Statistical analysis

For normal distribution with one independent variable experiments, unpaired *t*-test or one-way ANOVA analysis was used, while two-way ANOVA was used for the data with more than one independent variable. For nonlinear data, the correlation between the data sets computed using Pearson's correlation coefficients to determine the extent of statistical relationship using *P*-value (Two-tailed test). Level of significance was represented in the form of *P*-value (**P* < 0.05; ***P* < 0.01; ****P* < 0.001; *****P* < 0.0001). All plots, unless stated otherwise, were plotted in the GraphPad Prism 9.

Data availability

Computational models, HDX-MS data, plasmids, antibodies and worms generated by the authors will be distributed upon request to other researchers. The mass spectrometry proteomics data were deposited to the ProteomeXchange Consortium via the PRIDE partner repository with the dataset identifier PXD028023 (Perez-Riverol *et al*, 2019), and are accessible at <http://proteomecentral.proteomexchange.org/cgi/GetDataset?ID=PX028023>

Expanded View for this article is available online.

Acknowledgements

We thank the Caenorhabditis Genetics Center (funded by the NIH National Center for Research Resources, P40 OD010440) for strains and Addgene for plasmids. We thank the Biophysics and Structural Biology Facility (RRID:SCR_021630) and the Genome Engineering Unit of the International Institute of Molecular and Cell Biology in Warsaw for SPR analysis and generation of DNA constructs, respectively. We thank Marta Niklewicz for her technical assistance. We thank Vishnu Balaji and Gabriele Stellbrink of the Hoppe laboratory for discussions and technical support and members of the Pokrzywa laboratory for discussions and comments on the manuscript.

Work in the W.P. laboratory was funded by the Foundation for Polish Science, cofinanced by the European Union under the European Regional Development Fund (grant POIR.04.04.00-00-5EAB/18-00) and additionally supported by the National Science Center, Poland (grant 2016/23/B/NZ3/00753 and 2021/41/N/NZ1/03086). The research was also supported by the International Institute of Molecular and Cell Biology in Warsaw under an internal collaborative project fund. The equipment used for HDX-MS was sponsored by the National Multidisciplinary Laboratory of Functional Nanomaterials (POIGT.02.02.00-00-025/09-00). Work in the T.H. laboratory was funded by the Deutsche Forschungsgemeinschaft (DFG, German Research Foundation) under Germany's Excellence Strategy – EXC 2030 – 390661388, FKZ: ZUK81/1 and by the European Research Council (ERC-CoG-616499) to T.H. Diese Arbeit wurde von der Deutschen Forschungsgemeinschaft (DFG) im Rahmen der deutschen Exzellenzstrategie - EXC 2030 – 390661388, FKZ: ZUK81 / 1 und vom Europäischen Forschungsrat (ERC-CoG-616499) gefördert. Work in M.K. laboratory was supported by the German Research Foundation (DFG) as part of the

Excellence Strategy EXC 2030-390661388. C.J.C. and U.S. were funded by National Institute of Health grants R01-GM097082.

Author contributions

Aniruddha Das: Conceptualization; data curation; formal analysis; validation; investigation; visualization; methodology. **Pankaj Thapa:** Conceptualization; data curation; formal analysis; investigation; visualization; methodology.

Ulises Santiago: Formal analysis; visualization. **Nilesh Shanmugam:** Formal analysis; investigation. **Katarzyna Banasiak:** Formal analysis; investigation; visualization. **Katarzyna Dąbrowska:** Formal analysis; investigation. **Hendrik Nolte:** Formal analysis; investigation; visualization. **Natalia A Szulc:** Formal analysis; visualization. **Rose M Gathungu:** Investigation. **Dominik Cysewski:** Formal analysis. **Marcus Krüger:** Resources. **Michał Dadlez:** Resources.

Marcin Nowotny: Resources; supervision. **Carlos J Camacho:** Conceptualization; formal analysis. **Thorsten Hoppe:** Resources. **Wojciech Pokrzywa:** Conceptualization; resources; data curation; formal analysis; supervision; funding acquisition; validation; visualization; project administration.

Disclosure and competing interests statement

The authors declare that they have no conflict of interest.

References

- Ackermann L, Schell M, Pokrzywa W, Kevei É, Gartner A, Schumacher B, Hoppe T (2016) E4 ligase-specific ubiquitination hubs coordinate DNA double-strand-break repair and apoptosis. *Nat Struct Mol Biol* 23: 995–1002
- Alberti S, Böhse K, Arndt V, Schmitz A, Höhfeld J (2004) The chaperone HspBP1 inhibits the CHIP ubiquitin ligase and stimulates the maturation of the cystic fibrosis transmembrane conductance regulator. *Mol Biol Cell* 15: 4003–4010
- Alesekh S, Aharoni A, Brotman Y, Contrepois K, D'Auria J, Ewald JC, Ewald J, Fraser PD, Giavalisco P, Hall RD *et al* (2021) Mass spectrometry-based metabolomics: a guide for annotation, quantification and best reporting practices. *Nat Methods* 18: 747–756
- Arndt V, Daniel C, Nastainczyk W, Alberti S, Höhfeld J (2005) BAG-2 acts as an inhibitor of the chaperone-associated ubiquitin ligase CHIP. *Mol Biol Cell* 16: 5891–5900
- Ballinger CA, Connell P, Wu Y, Hu Z, Thompson LJ, Yin L-Y, Patterson C (1999) Identification of CHIP, a novel tetratricopeptide repeat-containing protein that interacts with heat shock proteins and negatively regulates chaperone functions. *Mol Cell Biol* 19: 4535–4545
- Bartel P, Chien CT, Sternglanz R, Fields S (1993) Elimination of false positives that arise in using the two-hybrid system. *Biotechniques* 14: 920–924
- Bhuripanyo K, Wang Y, Liu X, Zhou L, Liu R, Duong D, Zhao B, Bi Y, Zhou H, Chen G *et al* (2018) Identifying the substrate proteins of U-box E3s E4B and CHIP by orthogonal ubiquitin transfer. *Sci Adv* 4: e1701393
- Brenner S (1974) The genetics of *Caenorhabditis elegans*. *Genetics* 77: 71–94
- Buetow L, Huang DT (2016) Structural insights into the catalysis and regulation of E3 ubiquitin ligases. *Nat Rev Mol Cell Biol* 17: 626–642
- Cantoni GL (1975) Biological methylation: selected aspects. *Annu Rev Biochem* 44: 435–451
- Case DA, Ben-Shalom IY, Brozell SR, Cerutti DS, Cheatham TE III, Cruzeiro VWD, Darden TA, Duke RE, Ghoreishi D, Gilson MK (2018) *Amber 2018*. San Francisco, CA: University of California
- Christensen DE, Brzovic PS, Klevit RE (2007) E2-BRCA1 RING interactions dictate synthesis of mono- or specific polyubiquitin chain linkages. *Nat Struct Mol Biol* 14: 941–948

- Cortese MS, Baird JP, Uversky VN, Dunker AK (2005) Uncovering the unfoldome: Enriching cell extracts for unstructured proteins by acid treatment. *J Proteome Res* 4: 1610–1618
- Cox J, Mann M (2008) MaxQuant enables high peptide identification rates, individualized p.p.b.-range mass accuracies and proteome-wide protein quantification. *Nat Biotechnol* 26: 1367–1372
- Cox J, Neuhauser N, Michalski A, Scheltema RA, Olsen JV, Mann M (2011) Andromeda: a peptide search engine integrated into the MaxQuant environment. *J Proteome Res* 10: 1794–1805
- Dai Q, Qian SB, Li HH, McDonough H, Borchers C, Huang D, Takayama S, Younger JM, Ren HY, Cyr DM *et al* (2005) Regulation of the cytoplasmic quality control protein degradation pathway by BAG2. *J Biol Chem* 280: 38673–38681
- Depuydt G, Shanmugam N, Rasuloova M, Dhondt I, Braeckman BP (2016) Increased protein stability and decreased protein turnover in the *Caenorhabditis elegans* *ins/igf-1 daf-2* mutant. *J Gerontol Ser A Biol Sci Med Sci* 71: 1553–1559
- Evans R, O'Neill M, Pritzel A, Antropova N, Senior A, Green T, Žídek A, Bates R, Blackwell S, Yim J *et al* (2022) Protein complex prediction with AlphaFold-Multimer. *bioRxiv* <https://doi.org/10.1101/2021.10.04.463034> [PREPRINT]
- Faull SV, Lau AMC, Martens C, Ahdash Z, Hansen K, Yébenes H, Schmidt C, Beuron F, Cronin NB, Morris EP *et al* (2019) Structural basis of Cullin 2 RING E3 ligase regulation by the COP9 signalosome. *Nat Commun* 10: 3814
- Formstecher E, Aresta S, Collura V, Hamburger A, Meil A, Trehin A, Reverdy C, Betin V, Maire S, Brun C *et al* (2005) Protein interaction mapping: a *Drosophila* case study. *Genome Res* 15: 376–384
- Fromont-Racine M, Rain JC, Legrain P (1997) Toward a functional analysis of the yeast genome through exhaustive two- hybrid screens. *Nat Genet* 16: 277–282
- Gazda L, Pokrzywa W, Hellerschmied D, Löwe T, Forné I, Mueller-Planitz F, Hoppe T, Clausen T (2013) The myosin chaperone UNC-45 is organized in tandem modules to support myofilament formation in *C. elegans*. *Cell* 152: 183–195
- Goetz AW, Williamson MJ, Xu D, Poole D, Grand SL, Walker RC (2012) Routine microsecond molecular dynamics simulations with AMBER on GPUs. 1. Generalized born. *J Chem Theory Comput* 8: 1542–1555
- Graf C, Stankiewicz M, Nikolay R, Mayer MP (2010) Insights into the conformational dynamics of the E3 ubiquitin ligase CHIP in complex with chaperones and E2 enzymes. *Biochemistry* 49: 2121–2129
- Hänzelmann P, Stinglele J, Hofmann K, Schindelin H, Raasi S (2010) The yeast E4 ubiquitin ligase Ufd2 interacts with the ubiquitin-like domains of Rad23 and Dsk2 via a novel and distinct ubiquitin-like binding domain. *J Biol Chem* 285: 20390–20398
- Hatakeyama S, Yada M, Matsumoto M, Ishida N, Nakayama KI (2001) U box proteins as a new family of ubiquitin-protein ligases. *J Biol Chem* 276: 33111–33120
- Hellerschmied D, Roessler M, Lehner A, Gazda L, Stejskal K, Imre R, Mechtler K, Dammermann A, Clausen T (2018) UFD-2 is an adaptor-assisted E3 ligase targeting unfolded proteins. *Nat Commun* 9: 484
- Hoppe T, Cassata G, Barral JM, Springer W, Hutagalung AH, Epstein HF, Baumeister R (2004) Regulation of the myosin-directed chaperone UNC-45 by a novel E3/E4-multiubiquitylation complex in *C. elegans*. *Cell* 118: 337–349
- Huerta-Cepas J, Szklarczyk D, Heller D, Hernández-Plaza A, Forslund SK, Cook H, Mende DR, Letunic I, Rattei T, Jensen LJ *et al* (2019) EggNOG 5.0: A hierarchical, functionally and phylogenetically annotated orthology resource based on 5090 organisms and 2502 viruses. *Nucleic Acids Res* 47: D309–D314
- Hughes CS, Foehr S, Garfield DA, Furlong EE, Steinmetz LM, Krijgsveld J (2014) Ultrasensitive proteome analysis using paramagnetic bead technology. *Mol Syst Biol* 10: 757
- Imai Y, Soda M, Hatakeyama S, Akagi T, Hashikawa T, Nakayama KI, Takahashi R (2002) CHIP is associated with Parkin, a gene responsible for familial Parkinson's disease, and enhances its ubiquitin ligase activity. *Mol Cell* 10: 55–67
- Jiang J, Ballinger CA, Wu Y, Dai Q, Cyr DM, Höhfeld J, Patterson C (2001) CHIP is a U-box-dependent E3 ubiquitin ligase: Identification of Hsc70 as a target for ubiquitylation. *J Biol Chem* 276: 42938–42944
- Joshi V, Amanullah A, Upadhyay A, Mishra R, Kumar A, Mishra A (2016) A decade of boon or burden: What has the chip ever done for cellular protein quality control mechanism implicated in neurodegeneration and aging? *Front Mol Neurosci* 9: 93
- Kamadurai HB, Qiu Y, Deng A, Harrison JS, MacDonald C, Actis M, Rodrigues P, Miller DJ, Souphron J, Lewis SM *et al* (2013) Mechanism of ubiquitin ligation and lysine prioritization by a HECT E3. *elife* 2: e00828
- Kamath RS, Ahringer J (2003) Genome-wide RNAi screening in *Caenorhabditis elegans*. *Methods* 30: 313–321
- Kerscher O, Felberbaum R, Hochstrasser M (2006) Modification of proteins by ubiquitin and ubiquitin-like proteins. *Annu Rev Cell Dev Biol* 22: 159–180
- Kim K, Boo K, Yu YS, Oh SK, Kim H, Jeon Y, Bhin J, Hwang D, Il KK, Lee JS *et al* (2017) ROR α controls hepatic lipid homeostasis via negative regulation of PPAR γ transcriptional network. *Nat Commun* 8: 162
- Koegl M, Hoppe T, Schlenker S, Ulrich HD, Mayer TU, Jentsch S (1999) A novel ubiquitination factor, E4, is involved in multiubiquitin chain assembly. *Cell* 96: 635–644
- Koliopoulos MG, Esposito D, Christodoulou E, Taylor IA, Rittinger K (2016) Functional role of TRIM E3 ligase oligomerization and regulation of catalytic activity. *EMBO J* 35: 1204–1218
- Komander D (2009) The emerging complexity of protein ubiquitination. *Biochem Soc Trans* 37: 937–953
- Kuhlbrodt K, Mouysset J, Hoppe T (2005) Orchestra for assembly and fate of polyubiquitin chains. *Essays Biochem* 41: 1–14
- Liao Y, Wang J, Jaehnig EJ, Shi Z, Zhang B (2019) WebGestalt 2019: gene set analysis toolkit with revamped UIs and APIs. *Nucleic Acids Res* 47: W199–W205
- Liu C, Liu W, Ye Y, Li W (2017) Ufd2p synthesizes branched ubiquitin chains to promote the degradation of substrates modified with atypical chains. *Nat Commun* 8: 14274
- Liu J, Nussinov R (2011) Flexible cullins in cullin-RING E3 ligases allosterically regulate ubiquitination. *J Biol Chem* 286: 40934–40942
- Ly K, Reid SJ, Snell RG (2015) Rapid RNA analysis of individual *Caenorhabditis elegans*. *MethodsX* 2: 59–63
- Maier JA, Martinez C, Kasavajhala K, Wickstrom L, Hauser KE, Sönnichsen P (2015) ff14SB: improving the accuracy of protein side chain and backbone parameters from ff99SB. *J Chem Theory Comput* 11: 3696–3713
- Murata S, Minami Y, Minami M, Chiba T, Tanaka K (2001) CHIP is a chaperone-dependent E3 ligase that ubiquitylates unfolded protein. *EMBO Rep* 2: 1133–1138
- Narayan V, Landré V, Ning J, Hernychova L, Muller P, Verma C, Walkinshaw MD, Blackburn EA, Ball KL (2015) Protein-protein interactions modulate the docking-dependent E3-ubiquitin ligase activity of carboxy-terminus of Hsc70-interacting protein (CHIP). *Mol Cell Proteomics* 14: 2973–2987

- Nikolay R, Wiederkehr T, Rist W, Kramer G, Mayer MP, Bukau B (2004) Dimerization of the human E3 ligase CHIP via a coiled-coil domain is essential for its activity. *J Biol Chem* 279: 2673–2678
- Notredame C, Higgins DG, Heringa J (2000) T-coffee: a novel method for fast and accurate multiple sequence alignment. *J Mol Biol* 302: 205–217
- Page RC, Pruneda JN, Amick J, Klevit RE, Misra S (2012) Structural insights into the conformation and oligomerization of e2-ubiquitin conjugates. *Biochemistry* 51: 4175–4187
- Palmer JL, Abeles RH (1976) Mechanism for enzymatic thioether formation. Mechanism of action of S-adenosylhomocysteinase. *J Biol Chem* 251: 5817–5819
- Palmer JL, Abeles RH (1979) The mechanism of action of S-adenosylhomocysteinase. *J Biol Chem* 254: 1217–1226
- Paul I, Ghosh MK (2014) The E3 ligase CHIP: insights into its structure and regulation. *Biomed Res Int* 2014: 918183
- Perez-Riverol Y, Csordas A, Bai J, Bernal-Llinares M, Hewapathirana S, Kundu DJ, Inuganti A, Griss J, Mayer G, Eisenacher M et al (2019) The PRIDE database and related tools and resources in 2019: Improving support for quantification data. *Nucleic Acids Res* 47: D442–D450
- Petroski MD, Deshaies RJ (2005) Mechanism of lysine 48-linked ubiquitin-chain synthesis by the cullin-RING ubiquitin-ligase complex SCF-Cdc34. *Cell* 123: 1107–1120
- Puchała W, Burdukiewicz M, Kistowski M, Dąbrowska KA, Badaczewska-Dawid AE, Cysewski D, Dadlez M (2020) HaDeX: an R package and web-server for analysis of data from hydrogen-deuterium exchange mass spectrometry experiments. *Bioinformatics* 36: 4516–4518
- Rajalingam D, Loftis C, Xu JJ, Kumar TKS (2009) Trichloroacetic acid-induced protein precipitation involves the reversible association of a stable partially structured intermediate. *Protein Sci* 18: 980–993
- Richly H, Rape M, Braun S, Rumpf S, Hoeg C, Jentsch S (2005) A series of ubiquitin binding factors connects CDC48/p97 to substrate multiubiquitylation and proteasomal targeting. *Cell* 120: 73–84
- Riley BE, Loughheed JC, Callaway K, Velasquez M, Brecht E, Nguyen L, Shaler T, Walker D, Yang Y, Regnstrom K et al (2013) Structure and function of Parkin E3 ubiquitin ligase reveals aspects of RING and HECT ligases. *Nat Commun* 4: 1982
- Ryckaert JP, Ciccotti G, Berendsen HJC (1977) Numerical integration of the cartesian equations of motion of a system with constraints: molecular dynamics of n-alkanes. *J Comput Phys* 23: 327–341
- Salomon-Ferrer R, Götz AW, Poole D, Le Grand S, Walker RC (2013) Routine microsecond molecular dynamics simulations with AMBER on GPUs. 2. Explicit solvent particle mesh ewald. *J Chem Theory Comput* 9: 3878–3888
- Scaglione KM, Zavodszky E, Todi SV, Patury S, Xu P, Rodríguez-Lebrón E, Fischer S, Konen J, Djarmati A, Peng J et al (2011) Ube2w and Ataxin-3 coordinately regulate the ubiquitin ligase CHIP. *Mol Cell* 43: 599–612
- Schaefer JB, Morgan DO (2011) Protein-linked ubiquitin chain structure restricts activity of deubiquitinating enzymes. *J Biol Chem* 286: 45186–45196
- Scheufler C, Brinker A, Bourenkov G, Pegoraro S, Moroder L, Bartunik H, Hartl FU, Moarefi I (2000) Structure of TPR domain-peptide complexes: critical elements in the assembly of the Hsp70-Hsp90 multichaperone machine. *Cell* 101: 199–210
- Soss SE, Yue Y, Dhe-Paganon S, Chazin WJ (2011) E2 conjugating enzyme selectivity and requirements for function of the E3 ubiquitin ligase CHIP. *J Biol Chem* 286: 21277–21286
- Tatham MH, Plechanovová A, Jaffray EG, Salmen H, Hay RT (2013) Ube2w conjugates ubiquitin to α -amino groups of protein N-termini. *Biochem J* 453: 137–145
- Tawo R, Pokrzywa W, Kevei É, Akyuz ME, Balaji V, Adrian S, Höhfeld J, Hoppe T (2017) The ubiquitin ligase CHIP integrates proteostasis and aging by regulation of insulin receptor turnover. *Cell* 169: 470–482
- Tehlivets O (2011) Homocysteine as a risk factor for atherosclerosis: is its conversion to S-adenosyl-L-homocysteine the key to deregulated lipid metabolism? *J Lipids* 2011: 702853
- Di Tommaso P, Moretti S, Xenarios I, Orobítg M, Montanyola A, Chang JM, Taly JF, Notredame C (2011) T-Coffee: A web server for the multiple sequence alignment of protein and RNA sequences using structural information and homology extension. *Nucleic Acids Res* 39: W13–W17
- Tyanova S, Temu T, Sinitcyn P, Carlson A, Hein MY, Geiger T, Mann M, Cox J (2016) The Perseus computational platform for comprehensive analysis of (prote)omics data. *Nat Methods* 13: 731–740
- Visram M, Radulovic M, Steiner S, Malanovic N, Eichmann TO, Wolinski H, Rechberger GN, Tehlivets O (2018) Homocysteine regulates fatty acid and lipid metabolism in yeast. *J Biol Chem* 293: 5544–5555
- Vittal V, Wenzel DM, Brzovic PS, Klevit RE (2013) Biochemical and structural characterization of the ubiquitin-conjugating enzyme UBE2W reveals the formation of a noncovalent homodimer. *Cell Biochem Biophys* 67: 103–110
- Vitvitsky V, Mosharov E, Tritt M, Ataullakhanov F, Banerjee R (2003) Redox regulation of homocysteine-dependent glutathione synthesis. *Redox Rep* 8: 57–63
- Vojtek AB, Hollenberg SM (1995) Ras-Raf interaction: two-hybrid analysis. *Methods Enzymol* 255: 331–342
- Vrablik TL, Petyuk VA, Larson EM, Smith RD, Watts JL (2015) Lipidomic and proteomic analysis of *Caenorhabditis elegans* lipid droplets and identification of ACS-4 as a lipid droplet-associated protein. *Biochim Biophys Acta* 1851: 1337–1345
- Wang L, Liu YT, Hao R, Chen L, Chang Z, Wang HR, Wang ZX, Wu JW (2011) Molecular mechanism of the negative regulation of Smad1/5 protein by Carboxyl terminus of Hsc70-interacting protein (CHIP). *J Biol Chem* 286: 15883–15894
- Waterhouse A, Bertoni M, Bienert S, Studer G, Tauriello G, Gumienny R, Heer FT, De Beer TAP, Rempfer C, Bordoli L et al (2018) SWISS-MODEL: homology modelling of protein structures and complexes. *Nucleic Acids Res* 46: W296–W303
- Waterhouse AM, Procter JB, Martin DMA, Clamp M, Barton GJ (2009) Jalview version 2—a multiple sequence alignment editor and analysis workbench. *Bioinformatics* 25: 1189–1191
- Wenzel DM, Lissounov A, Brzovic PS, Klevit RE (2011) UBCH7 reactivity profile reveals parkin and HHARI to be RING/HECT hybrids. *Nature* 474: 105–108
- Wu HH, Wang B, Armstrong SR, Abuetabh Y, Leng S, Roa WHY, Atfi A, Marchese A, Wilson B, Sergi C et al (2021) Hsp70 acts as a fine-switch that controls E3 ligase CHIP-mediated TAp63 and Δ np63 ubiquitination and degradation. *Nucleic Acids Res* 49: 2740–2758
- Xu Z, Devlin KI, Ford MG, Nix JC, Qin J, Misra S (2006) Structure and Interactions of the helical and U-box domains of CHIP, the C terminus of HSP70 interacting protein. *Biochemistry* 45: 4749–4759
- Ye Z, Needham PG, Estabrooks SK, Whitaker SK, Garcia BL, Misra S, Brodsky JL, Camacho CJ (2017) Symmetry breaking during homodimeric assembly activates an E3 ubiquitin ligase. *Sci Rep* 7: 1789
- Zhang H, Amick J, Chakravarti R, Santarriaga S, Schlanger S, McGlone C, Dare M, Nix JC, Scaglione KM, Stuehr DJ et al (2015) A bipartite interaction between Hsp70 and CHIP regulates ubiquitination of chaperoned client proteins. *Structure* 23: 472–482
- Zhang H, Liu Z, Ma S, Zhang H, Kong F, He Y, Yang X, Wang Y, Xu H, Yang A et al (2016) Ratio of S-adenosylmethionine to S-adenosylhomocysteine as a sensitive indicator of atherosclerosis. *Mol Med Rep* 14: 289–300

Zhang M, Windheim M, Roe SM, Peggie M, Cohen P, Prodromou C, Pearl LH (2005) Chaperoned ubiquitylation—crystal structures of the CHIP U box E3 ubiquitin ligase and a CHIP-Ubc13-Uev1a complex. *Mol Cell* 20: 525–538



License: This is an open access article under the terms of the Creative Commons Attribution License, which permits use, distribution and reproduction in any medium, provided the original work is properly cited.